2009

Novel Ultrasound Elastography Imaging System for Breast Cancer Assessment

Hirad Karimi
Western University

Novel Ultrasound Elastography Imaging System for Breast Cancer Assessment

(Spine title: Novel Ultrasound Elastography for Breast Cancer Assessment)

(Thesis Format: Monograph)

By

Hirad Karimi

Graduate Program in Engineering Science

Department of Electrical and Computer Engineering

A thesis submitted in partial fulfillment of the requirements for the degree of Master of Engineering Science

School of Graduate and Postdoctoral Studies

The University of Western Ontario

London, Ontario, Canada

THE UNIVERSITY OF WESTERN ONTARIO

SCHOOL OF GRADUATE AND POSTDOCTORAL STUDIES

CERTIFICATE OF EXAMINATION

Supervisors	Examiners
Dr. Abbas Samani	Thomas Jenkyn
Dr. Aaron Fenster	James Lacefield
	Roy Eagleson

The thesis by

Hirad Karimi

entitled:

Novel Ultrasound Elastography Imaging System for Breast Cancer Assessment

is accepted in partial fulfillment of the

requirements for the degree of

Master of Engineering Science

Date _____ _____

Chair of the Thesis Examination Board

Abstract

Most conventional methods of breast cancer screening such as X-ray, Ultrasound (US) and MRI have some issues ranging from weaknesses associated with tumour detection or classification to high cost or excessive time of image acquisition and reconstruction. Elastography is a non-invasive technique to visualize suspicious areas in soft tissues such as the breast, prostate and myocardium using tissue stiffness as image contrast mechanism. In this study, a breast Elastography system based on US imaging is proposed. This technique is fast, expected to be cost effective and more sensitive and specific compared to conventional US imaging. Unlike current Elastography techniques that image relative elastic modulus, this technique is capable of imaging absolute Young's modulus (YM). In this technique, tissue displacements and surface forces used to mechanically stimulate the tissue are acquired and used as input to reconstruct the tissue YM distribution. For displacements acquisition, two techniques were used in this research: 1) a modified optical flow technique, which estimates the displacement of each node from US pre- and post-compression images and 2) Radio Frequency (RF) signal cross-correlation technique. In the former, displacements are calculated in 2 dimensions whereas in the latter, displacements are calculated in the US axial direction only. For improving the quality of elastography images, surface force data was used to calculate the stress distribution throughout the organ of interest by using an analytical model and a statistical numerical model. For force data acquisition, a system was developed in which load cells are used to measure forces on the surface of the breast. These forces are input into the stress distribution models to estimate the tissue stress distribution. By combining the stress field with the strain field calculated from the acquired displacements using Hooke's law, the YM can be reconstructed efficiently. To validate the proposed technique, numerical and tissue mimicking phantom studies were conducted. For the numerical phantom study, a 3D breast-shape phantom was created with synthetic US pre- and post-compression images where the results showed the feasibility of reconstructing the absolute value of YM of tumour and background. In the tissue mimicking study, a block shape gelatine-agar phantom was constructed with a cylindrical inclusion. Results obtained from this study also indicated reasonably accurate reconstruction of the YM. The quality of the obtained elasticity images shows that image quality is improved by incorporating the adapted stress calculation techniques. Furthermore, the proposed elastography system is reasonably fast and can be potentially used in real-time clinical applications.

Keywords: Breast Cancer, Elastography, Optical Flow, Ultrasound Imaging, Young's Modulus, Inverse Problem

Dedication

To my lovely family and friends for their excessive and unconditional support throughout my entire life

Acknowledgments

I would like to take this opportunity to appreciate my supervisors, Dr. Abbas Samani and Dr. Aaron Fenster, for giving me the opportunity to join and collaborate with their research group during past two years. The accomplishments of this project would not have been possible without their extensive and dedicated support and encouragements.

I also would like to thank Marc Cicero for helping us in designing mechanical parts of force data acquisition system.

I also would like to thank my colleagues at Dr. Samani's Lab who helped me with all aspect of my work and providing such a friendly environment to work in during past two years.

Table of Contents

List of Figures

1. Introduction

1.1. Cancer

Cancer is a group of diseases in which a number of cells are associated with uncontrolled growth, invasion (infecting adjacent tissues), and sometimes metastasis (spreading to other organs in the body via blood). These three properties of cancers distinguish them from benign tumours, which are self-limited, and do not invade or produce metastasis. Most cancers create a tumour but some, like leukemia, do not.

Cancer may occur in people at all ages, even in infant, but the risk for most varieties increases with age. According to the Canadian Cancer Society, almost 171000 people will be diagnosed with cancer and about 75300 deaths will die of it in year 2009.

Almost all cancers are caused by abnormalities in cells growth. These abnormalities may be caused by carcinogens, such as tobacco smoke, radiation or chemicals. Other types of cancers may be caused by irregular replication in DNA, or are inherited, and therefore present in all cells since birth. In many diagnostic procedures, first, images are taken of the organ to detect any abnormality in the organ. If an abnormality is present, a radiologist removes samples of the suspicious tissue using a procedure called biopsy. Some cancer types can be treated and cured. Treatment depends on the specific type, location, and stage of the cancer. Once cancer is diagnosed, it is usually treated with a combination of procedures such as surgery, chemotherapy and radiotherapy. Many researches work specifically on treatment methods of a type of cancer. Research has led to significant progress in the development of therapies such as brachytherapy where radioactive seeds are inserted in cancerous tissues to kill cancerous cells. Effective cancer treatment usually requires early diagnosis. Medical imaging techniques ranging from X-ray to PET (Positron Emission Tomography) are very effective for diagnosis. For example Figure 1-1 shows a cancerous lump in a lung seen on an X-ray image.

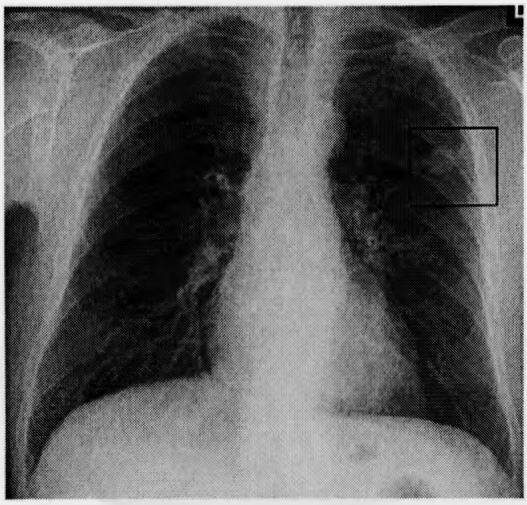

Figure 1-1: Chest X-Ray showing lung cancer in a left lung (courtesy of Canadian Cancer Society)

1.2. Breast Anatomy

The breast is a volume of fibroglandular and adipose tissues. The adipose tissue is extended throughout the breast, which forms its shape. The fibroglandular tissues of the breast are responsible for producing milk. Milk is produced in the alveoli, which are small clusters of cells. The produced milk moves down to the nipple via the ducts as shown in Figure 1-2.

As depicted in Figure 1-2, the breast is composed of:

- Fibro glandular tissues that are responsible to produce milk
- Nipple
- Ducts that transfer the milk from the aveoli to the nipple
- Areola
- Connective tissue that surrounds the glands and ducts
- Fatty tissues

Arteries carry blood which contains oxygen from the heart to the chest wall and the breasts while veins carry de-oxygenated blood back to the heart. The arteries located within the breast extend from vessels in the neck and feed the interior parts of the breast. The auxiliary artery feed posterior parts of the breast with blood.

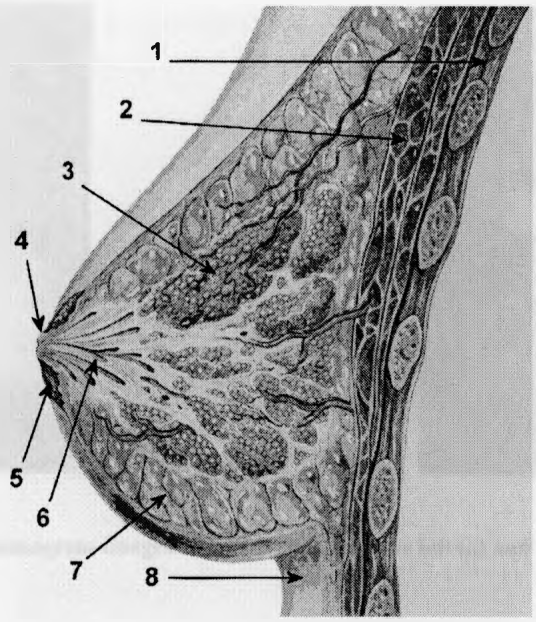

Figure 1-2: female breast diagram- Legend: 1-Chest wall 2-Pectoralis muscles 3-Lobules 4-Nipple 5-Areola 6-Duct 7-Fatty tissue 8-Skin

1.3. Breast Cancer

Breast cancer is a cancer that starts in the breast due to abnormality in breast tissues. There are different types of breast cancer, with different stages, invasiveness, and genetic structure. With treatment, 10-year disease-free survival varies from 10% to 98%. Treatment includes surgery, drugs (chemotherapy), radiation and brachytherapy.

Based on statistics presented by the Canadian Cancer Society, breast cancer is the third most common type of cancer occurrence in year 2009 in Canada after lung and prostate cancer. It is estimated that 22900 people including both sexes will be diagnosed with breast cancer in this year. It is also estimated that almost 5400 people will die as a result of breast cancer.

Breast cancer is more frequent among women rather than men, but survival rates are identical for both sexes. Figure 1-3 shows a normal breast on the left and a cancerous breast on the right. Usually micro-calcification visible in X-ray mammograms is an indication of malignant area in the breast [47].

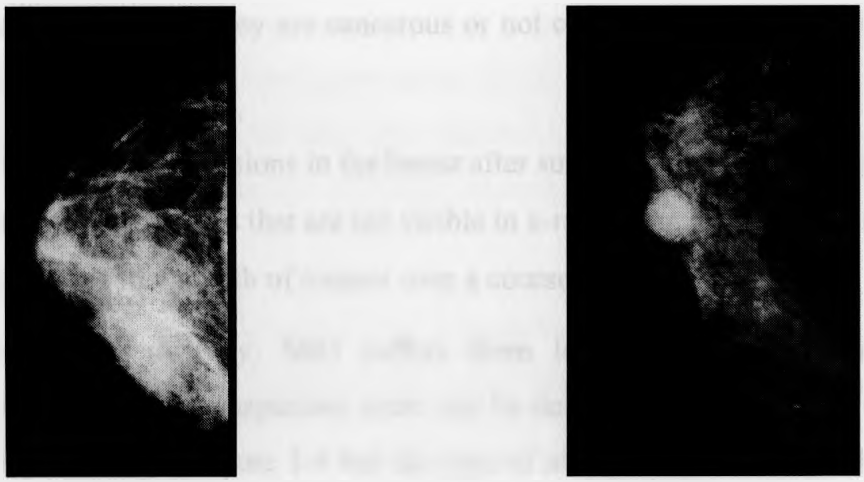

(a) (b)

Figure 1-3: X-ray Mammogram images of normal tissue on the left (a) and cancerous one on the right (b)

1.4. Screening Methods

Some screening methods are used because they have been shown to be helpful in early detection of cancers. These tests are shown to be capable of screening cancer in the organ, however, it has not been proven that these tests lead to reduction in rates of death caused by the cancer.

Scientists have been developing screening methods that are shown to be helpful in reducing the mortality rate. Assessment of such screening methods involve showing whether the screening method is capable of detecting cancer (before it produces symptoms) leading to reduction in mortality rate. Early detection of cancer may be helpful in order to conduct proper treatments and ultimately cure the cancer. Some of the most common methods used in screening cancer will be described in following sections.

1.4.1. MRI (Magnetic Resonance Imaging)

MRI is an imaging technique that uses a magnet, Radio Frequency (RF) coils, and a computer to reconstruct the image of areas inside the body. In the medium stage of breast cancer, MRI can be used for detection. At very advanced stages of the cancer, MRI has shown to be effective in detecting cancer in comparison with X-ray mammography. Most

of suspicious areas whether they are cancerous or not can be visualized in MRI images. MRI may be used to:

- Study leftover of lesions in the breast after surgery or radiation therapy.
- Study breast lesions that are not visible in x-ray mammography or ultrasound.
- Assessing the growth of tumour over a course of time.

While it has high sensitivity, MRI suffers from low specificity and being time demanding. In other words, suspicious areas can be detected by MRI images with high certainty as it is shown in Figure 1-4 but the type of abnormality cannot be determined confidently.

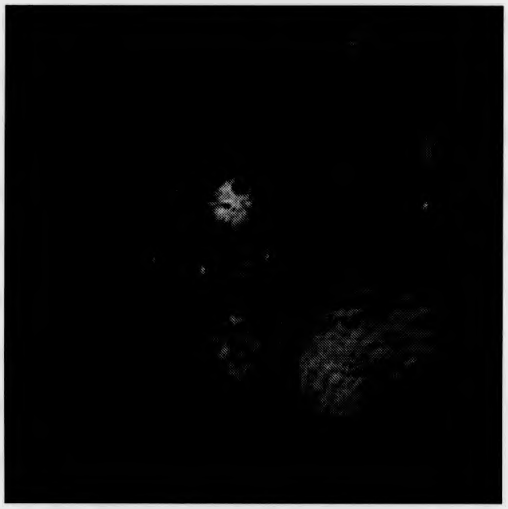

Figure 1-4: Breast MRI image that indicates a suspicious area(courtesy of Canadian Cancer Society)

1.4.2. Mammography

Mammography is an imaging technique that uses low-amplitude X-rays (usually around 0.7 mSv) to screen the human breast, and is used as a diagnostic as well as a screening technique. The main application of mammography is to detect breast cancer at early stages, typically through detection of presence of micro-calcifications. It has been shown that mammography is capable of reducing cancer related death rate. Except for breast self examination or palpation test in clinics, no other imaging techniques are shown to reduce

the risk of cancer mortality. Mammography has a false-negative (missed cancer) rate resulting from overlapping of fatty tissue on the micro-calcifications. In such situations, MR mammography would be an alternative choice for early cancer detection. Breast palpation can also be an effective screening technique provided that the tumour is superficial.

To acquire X-ray mammography, the breast is compressed by a mammography machine to increase image quality, and to prevent the breast from moving. Two images are taken from top and side view.

1.4.3. Diagnostic Sonography

Ultrasound (US) refers to sound waves with a frequency greater than the upper limit frequency that can be heard by humans. The lower frequency limit of ultrasound wave is usually taken to be 20 kHz. Medical ultrasound machines generate ultrasound waves sent through soft tissues to carry information about the tissue structure. The ultrasound waves generated by these machines are produced by piezoelectric components implanted in their probe. The reflection of sound waves is then captured to form ultrasonic images. Ultrasound imaging is usually used to acquire images of fetus in women's womb. It is also used to visualise blood vessels, muscles or tendons as well as abnormalities in organs such as the prostate or breast. Because ultrasound imaging is a real-time procedure, it is often used for image-guided procedures such as biopsy of masses for cytology or lung brachytherapy, etc.

There are several applications for ultrasound imaging. As for our purpose in this project, we refer to some of its applications in breast sonography.

- **Determining the type of a breast abnormality**

  The primary application of ultrasonic procedure in this context is to determine the type of the lump and find whether it is a solid tumour or a liquid filled cyst. Simple cysts are normally visible as dark areas in ultrasonic images. Methods such as Elastography have been developed based on ultrasound imaging to improve the diagnostic aspect of ultrasound.

- **Breast cancer screening**

  Another application of ultrasound is to screen the breast for any type of cancer or cyst. Cysts are normally shown by dark area as they consist of liquid which reduces the back propagation of the RF waves. Some types of tumours are hyper echoic which are highly bright areas in ultrasound images. However, there are types of lesions with back propagation properties that do not differ from normal tissues.

- **Ultrasound-guided breast biopsy**

  If a physician fails to detect breast tissue abnormality using imaging, s/he may choose to perform an ultrasound-guided biopsy. Because ultrasound provides real-time images, it is often used for image-guided biopsy procedures as well as image-guided therapies such as brachytherapy.

1.4.4. Self-Examination

Breast self-examination (BSE) is a simple method of screening abnormalities of the breast. It can be an effective tool for early detection of breast cancer especially if the tumour is superficial. The method involves the woman looking for any possible stiff area by palpating her breast or for any deformation of the breast. This is usually repeated in several positions, such as while having hands on the hips, and then again with arms held overhead. Breast self-examination (BSE) is known to be effective in early detection of any suspicious lesions along with mammography. While suitable for lesions located near the surface of the breast, BSE is not reliable with tumours located deeper in the tissue.

1.5. Diagnosis and Treatment Methods

Although screening methods are useful to detect abnormalities in the breast, further examinations are required to specify whether the detected lesion is benign or malignant.

1.5.1. Diagnosis

In the clinic, breast cancer is often diagnosed using a three-stage procedure. First, breast self-examination is conducted by a physician. Second, the patient is sent to X-ray

mammography for micro-calcification presence assessment. The final step is to perform a biopsy to remove tissue samples for further tests.

Biopsy is a medical examination in which a pathologist removes a sample of tissue for oncology assessments. By removing the samples from living tissue, cancer can be diagnosed effectively. There are three types of biopsy that can be conducted for assessing breast cancer:

- Excisional biopsy: in this type of biopsy, the entire lesion or suspicious area is removed.
- Core Biopsy or Incisional biopsy: this is a procedure in which a pathologist removes samples of the lesion or suspicious areas to examine under the microscope.
- Fine Needle Aspiration: this is a procedure of removing liquid samples from tissues or cysts without preserving the histological architecture of the tissue cells.

1.5.2. Treatments

There are several methods such as surgery, chemotherapy, radiation therapy or other methods to treat breast cancer. The choice of therapy depends on the position of lesion as well as the stage of the cancer. An ideal treatment method should involve removing the cancerous tissue without harming other parts of the body or the breast itself.

One treatment method is surgery, which has its own drawbacks. Following surgery, sometimes a microscopic portion of the cancerous tissue may remain in the breast. This may lead to recurrence or metastasis in other parts of the body, thus rendering the treatment ineffective. Radiation can also cause damage to surrounding tissues. The effectiveness of chemotherapy is sometimes limited by toxicity to the body.

1.6. Elastography

It is well known that alternation of tissue stiffness and presence of pathology are correlated. In other words, pathology may alter tissue stiffness. For example, in the

breast, a significant fraction of breast cancers are detected by the patient using BSE. Digital Rectal Exam (DRE) is another tissue palpation method clinically used for detecting prostate cancer. Detection by palpation, however, is limited to large tumours or small ones that are located near the surface of the organ of interest. If the lump is located deep inside the organ, it may not be detected by palpation[23].

Based on the concept of tissue palpation, a non-invasive technique called Elastography has been developed in the 1980s. Elastography has been shown to be capable of imaging local elasticity in experiments involving tissue mimicking phantoms, *ex vivo* and *in vivo* tissue. When a tissue volume is mechanically excited with a quasi-static or harmonic compression, the tissue deformation and internal stresses are defined by the boundary conditions as well as by the structure and properties of the tissue. In order to completely understand the local elastic properties of the tissue volume, it is necessary to estimate the stresses and measure the resulting tissue displacements in three orthogonal spatial directions.

Based on the applied mechanical excitation, there are two types of elastography methods:

- Quasi-Static Elastography
- Harmonic Elastography

1.6.1. Quasi-Static Elastography

In Quasi-Static Elastography, the mechanical stimulation applied to the soft tissue region of interest is either static or has very low frequency (0-5Hz)[26]. Displacements data induced by the mechanical stimulation are acquired using either US RF signals, MRI phase imaging, or other image processing techniques. The computed tissue displacements can be used directly to estimate tissue elasticity normally characterized by Young's Modulus (YM). This type of elastography is suitable for organs, which are easily accessible for mechanical stimulation, such as the breast or prostate.

1.6.2. Harmonic Elastography

In harmonic elastography, the mechanical excitation is a harmonic compression applied on the surface of the tissue and the tissue response is characterized by velocity of induced oscillating displacements. While quasi-static elastography is only capable of imaging tissue stiffness, harmonic elastography can image both tissue viscosity as well as stiffness parameters. These parameters can be reconstructed using the wave equations, which govern the waves propagated throughout the tissue volume. These parameters can be used for diagnosis purposes.

1.7. Thesis Objectives

As previously discuss, cancer alters tissue stiffness significantly leading to significant alteration in the tissue deformation pattern. This alternation can be captured using different imaging modalities such as MRI or US. Tissue response in quasi-static elastography can be characterized by local displacements using pre- and post-compression images. In MRI tissue displacements are computed using acquired phase data while with US they are computed using either visual motion inspection or RF signal cross-correlation. These displacements data are then used for reconstructing tissue viscoelastic properties in elastography techniques.

Since the 1980s, Elastography techniques have been developed and many methods have been proposed to improve the quality of elastography images. Elastography image shows tissue elasticity distribution within the region being examined. Many of the developed elastography techniques suffer from drawbacks such as being time demanding, having low signal-to-noise ratio (SNR), having image artefacts, etc. In this project, a novel technique based on US imaging is proposed with the aim of improving the quality of reconstructed elastography images.

In this proposed breast elastography technique, US imaging has been chosen as the imaging modality since it has some advantages over MRI. US is a real-time imaging modality that can be used in applications such as image-guided biopsy and therapy. Also,

if successful for developing a cancer detection and diagnosis technique, US based elastography would be significantly less expensive and more accessible in clinics.

In the techniques proposed in this thesis, compared to conventional elastography methods, additional information is incorporated to develop a real-time technique for reconstructing the absolute value of YM and also to improve the reconstruction accuracy. To the best of our knowledge, many conventional US Elastography (USE) techniques are capable of reconstructing the ratio of YM of a suspicious area to the YM of surrounding tissue only. A force data acquisition system has been designed and constructed to measure the forces applied on the surface of tissue. This data is incorporated into a statistical finite element method for computing the stress distribution within the region of interest.

Our main objective is to develop a real-time technique that can ultimately be used in clinical applications to reduce the number of patients who are referred to biopsy. This can be done by developing a technique capable of detecting and classifying suspicious areas in the organ of interest.

2. Literature Review

2.1. Theory of Elasticity

Continuum mechanics asserts that although a medium such as soft tissue is comprised of a hierarchy of smaller discrete building blocks (e.g. atoms, molecules, proteins, etc.) its mechanical behaviour can be characterized accurately by prescribing macroscopic field properties to the body. As a result of undergoing mechanical stimulation, the deformation of a continuum is governed by equations of equilibrium, strain-displacement, and a material constitutive law. The force balance equation of a continuum undergoing mechanical stimulation is:

$$\sigma_{ij,i} + \rho_0 b_i = \rho_0 u_j \qquad \text{Eq. 2-1}$$

where σ_{ij} denotes the Cauchy stress tensor, ρ_0 is the mass density, b_i is the body force distribution (per unit mass), and u_j are the components of displacement vector $\boldsymbol{u} = (u_x, u_y, u_z)$. The nine components of Cauchy stress tensor σ_{ij} are the three normal stresses$\sigma_{11}, \sigma_{22}, \sigma_{33}$ and six shear stresses $\sigma_{12}, \sigma_{21}, \sigma_{13}, \sigma_{31}, \sigma_{23}, \sigma_{32}$ as shown in Figure 2-1.

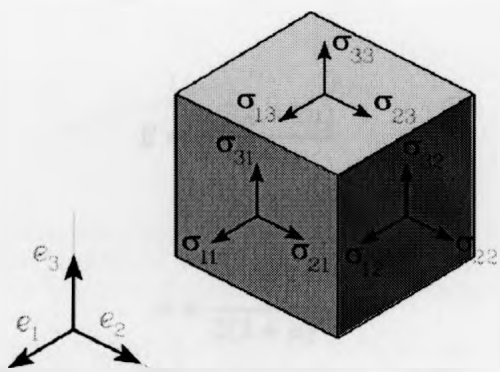

Figure 2-1: The Cauchy stress tensor

The mechanical properties of continua can be written mathematically using the constitutive equation for linear elastic behaviour that describes the stress strain relationship of the material:

$$\sigma_{ij} = C_{ijkm}\varepsilon_{km} \qquad \text{Eq. 2-2}$$

The C_{ijkm} coefficients of Eq. 2-2 (also referred to as the generalized Hook's Law) describe a linear relationship between the stress (σ_{ij}) and the strain (ε_{ij}) tensors at every point in a body. The strain tensor ε_{ij} is related to the displacement vector u_j through following equation:

$$\varepsilon_{ij} = \frac{1}{2}\,(u_{i,j} + u_{j,i}) \qquad \text{Eq. 2-3}$$

Because of symmetries in the stress tensor ($\sigma_{ij} = \sigma_{ji}$) and the assumption that the material is homogeneous and isotropic, only two independent constants are required to define C_{ijkm} and Eq. 2-2 reduces to:

$$\sigma_{ij} = \lambda\delta_{ij}\varepsilon_{kk} + 2\mu\varepsilon_{ij} \qquad \text{Eq. 2-4}$$

which is Hook's law for isotropic linear elastic materials. The δ_{ij} operator is known as the Kronecker delta where $\delta_{ii} = 1$ and $\delta_{ij} = \delta_{ji} = 0$ for i≠j. The two independent constants λ and μ are known as the Lame's constants. Rearranging Eq. 2-3 and expressing it in terms of the strain tensor ε_{ij} produces the following expression:

$$\varepsilon_{ij} = \frac{1}{E}\,[(1+\nu)\sigma_{ij} - \nu\delta_{ij}\sigma_{kk}] \qquad \text{Eq. 2-5}$$

where

$$E = \frac{\mu(3\lambda + 2\mu)}{\lambda + \mu} \qquad \text{Eq. 2-6}$$

and

$$\nu = \frac{\lambda}{2(\lambda + \mu)} \qquad \text{Eq. 2-7}$$

E and ν are known, respectively, as Young's Modulus and Poisson's ratio. For isotropic, elastic materials, these two parameters fully characterize the mechanical properties of the material. The Lame' constant μ is the shear modulus. For an isotropic, linear elastic material, the shear modulus is related to the Young's Modulus by the equation:

$$\mu = \frac{E}{2(1+\nu)} \qquad \text{Eq. 2-8}$$

The Young's Modulus is a measure of the stiffness of a material and it is defined as the rate of change of stress with strain. The Poisson's ratio is the ratio of the relative

transverse strain (normal to the applied load) to the corresponding extension strain in the direction of the applied load. Incompressible materials, such as biological soft tissues, have a Poisson's ratio close to 0.50. The shear modulus is a measure of a material's rigidity.

For linear-elastic materials, the Young's Modulus is constant over a range of strains. Within the strain range of 0 to 4%, breast tissue is often approximated as being linear elastic (Figure 2-2) with a Young's Modulus of approximately 3.125kPa (Wellman 1999 [46]). Over the same range of strains the Young's Modulus of breast cancer can be as high as 15.625kPa (five times stiffer). Beyond strains of 4% breast tissue begins to exhibit non-linear mechanical behaviour typical of biological soft tissues [26].

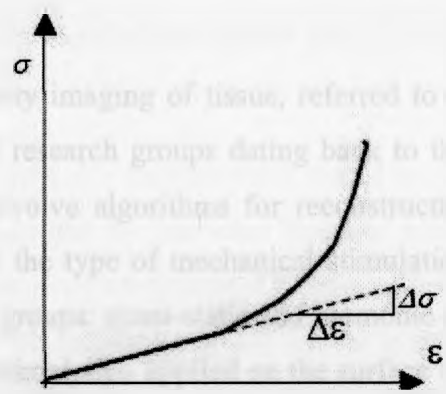

Figure 2-2: A typical stress-strain curve for soft tissue. Below strains of 4% the slope is relatively constant and the tissue can be idealized as linear elastic. Above strains of 4% the slope is not constant and the linear elasticity idealization is no longer valid.

Solving Eq. 2-1 to Eq. 2-3 provides the forward solution to the Elastography inverse problem. The forward solution is used to calculate the displacements $u(x_i)$ resulting from mechanical stimulation of soft tissue volume with a known Young's Modulus distribution $E(x_i)$.

The governing equations are often rearranged before they are solved. This is especially true for dynamic problems in elasticity, which retain all the time dependent terms. By substituting Eq. 2-4 into Eq. 2-1, and eliminating the strain using Eq. 2-3, the balance

equation can be expressed in terms of the displacements using the simplified Navier equation of elasticity:

$$\frac{\mu}{1-2\nu}u_{k,ki} + \mu u_{i,kk} + \rho_0 b_i = \rho_0 u_{i,tt} \qquad \text{Eq. 2-9}$$

With the help of Eq. 2-8, the Navier equation can also be expressed in terms of E and ν as follows:

$$\frac{E}{2(1-2\nu)(1+\nu)}u_{k,ki} + \frac{E}{2(1+\nu)}u_{i,kk} + \rho_0 b_i = \rho_0 u_{i,tt} \qquad \text{Eq. 2-10}$$

Eq. 2-10 is not suitable for compressible materials since it will become unstable as the Poisson's ratio approaches 0.50. Although soft tissues are nearly incompressible, in order to ensure a stable solution to Eq. 2-10, the Poisson's ratio is usually set to 0.495.

2.2. Elastography

Various methods of elasticity imaging of tissue, referred to as elastography, have been developed by a number of research groups dating back to the eighties [23][25][30-32]. Elastography techniques involve algorithms for reconstructing tissue elastic parameter distribution. Depending on the type of mechanical stimulation, elastography techniques are divided into two major groups: quasi-static and harmonic elastography. In quasi-static Elastography, mechanical stimulation applied on the surface of the medium is static or at a low frequency. In harmonic elastography, the mechanical stimulation is oscillatory with higher frequency (>40Hz). In most of elastography techniques, an inverse solution is computed to find the tissue elastic parameter distribution in the organ of interest using the tissue displacements resulting from the mechanical stimulation as input. Forward and inverse problems involved in typical elastography techniques will be described in the following section.

2.2.1. Forward and Inverse Problem

A forward problem is a mathematical model, which predicts the response of a stimulated system based on its known structure. For example, if an electric circuit is composed of known electric components with known connections, its output can be predicted for any known input. This prediction may involve analytical or numerical models that describe

the circuit's response. Figure 2-3 illustrates the forward model of a circuit used to find its output voltage.

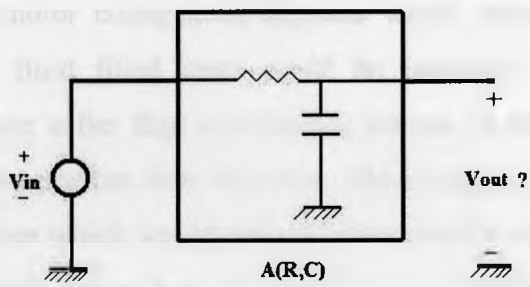

Figure 2-3: A forward model of RC circuit

By knowing the internal structure of the system A(R, C) and input V_{in}, we are able to compute V_{out} numerically.

In contrast, an inverse problem is a mathematical model or algorithm, which can predict the internal structure of a system by knowing its input and corresponding output. For example, if we know the input of an electrical system and its corresponding output, we may be able to determine the internal structure of the system. Figure 2-4 illustrates an inverse model concept to find the internal structure of the system.

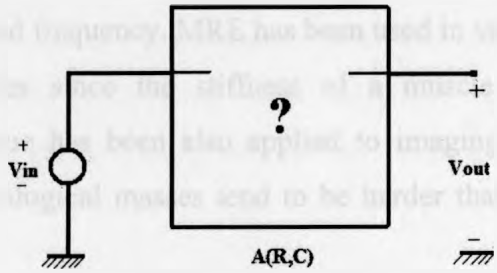

Figure 2-4: An inverse model schematic of an RC circuit

2.2.2. Application in assessing stiffness of biological tissues

Changes in tissue elasticity are generally correlated with the presence of pathology. Many breast cancer types are considerably stiffer than normal breast tissues. Other breast diseases involve fatty and/or collagenous deposits which increase or decrease tissue elasticity. Complicated fluid filled cysts could be invisible in standard ultrasound examinations, yet be quite softer than surrounding tissues. In many cases small lesions located deep in the breast prevent their detection. Moreover, the lesion may or may not have backscatter properties which would make it ultrasonically visible. In the last several years, a number of research groups have developed various techniques for measuring and imaging soft tissue stiffness.

In addition to US imaging, other imaging modalities have been used to image tissue elasticity. For example MRI based Elastography involves magnetic resonance imaging (MRI) used to acquire tissue displacements. Magnetic Resonance Elastography (MRE) usually refers to harmonic elastography where MRI is used to measure the wave field propagating through the tissue. This technique employs standard MRI scanner with a few modifications in addition to a vibrating metal plate placed on the skin for tissue stimulation. The simplest form of MRE works by measuring the wavelength distribution of the vibrations sent through the tissues. Pulsing the magnetic field in the MRI scanner in tune with the mechanical vibrations freezes the pattern of waves, permitting the wavelength to be measured. The elasticity of the tissue can then be calculated using the measured wavelengths and frequency. MRE has been used in various applications such as studying skeletal muscles since the stiffness of a muscle changes during muscle contraction. The technique has been also applied to imaging breast cancer and other cancer types where pathological masses tend to be harder than the surrounding normal tissue [10][26].

2.2.3. Principal Components of Elastography

As mentioned in section 1.6, in elastography, the tissue region of interest (ROI) is stimulated by either mechanical stimulator or in the case of USE, with the US probe. During tissue stimulation tissue displacement data, $u_i(x_i)$ induced by the stimulation is

acquired for each point within the ROI. In quasi-static elastography equations 2-1, 2-2 and 2-3 are applied in order to reconstruct Young's Modulus distribution within the ROI corresponding to the measured displacement data $u_i(x_i)$.

If the stress distribution induced by the mechanical stimulation within the tissue ROI is uniform or known, the ratio of Young's Modulus of a lesion to surrounding normal tissues can be estimated directly from the strain tensor ε_{ij}. The values of strain components are computed using spatial derivative of the displacement data $u_i(x_i)$. For example, if ε_{ij}^0 and ε_{ij}^n are strain components at point x_i^0 and x_i^n, which represent normal and suspicious tissues, respectively, the following relationship can be established between the Young's Modulus of normal and cancerous tissues using Eq. 2-5:

$$\frac{E^n}{E^0} = \frac{\frac{1}{\varepsilon_{ij}^n}[(1+\nu)\sigma_{ij}^n - \nu\delta_{ij}\sigma_{ij}^n]}{\frac{1}{\varepsilon_{ij}^0}[(1+\nu)\sigma_{ij}^0 - \nu\delta_{ij}\sigma_{ij}^0]} \qquad \text{Eq. 2-11}$$

If the stress distribution is uniform throughout the region of interest (i.e. $\sigma_{ij}^n = \sigma_{ij}^0$), Eq. 2-11 can be rewritten as follow:

$$\frac{E^n}{E^0} = \frac{\varepsilon_{ij}^0}{\varepsilon_{ij}^n} \qquad \text{Eq. 2-12}$$

It means that the ratio of the Young's Modulus at two points located in the normal tissue and suspicious area is proportional to the reciprocal ratio of strain components at the points. In most practical cases this assumption is not valid since we have finite medium where stress components have significant spatial variations especially when the medium contains inclusion. Therefore, estimating the ratio of Young's Modulus using Eq. 2-12 is not sufficiently accurate.

To accurately estimate Young's modulus ratio stress non-uniformity has to be taken into account. There are several approximate analytical methods for computing stress components throughout the ROI's volume provided that the compressive load on the surface of ROI is known. One of these methods is Boussinesq problem model where the geometry is considered to be semi-infinite and the material is assumed to be

homogeneous. The accuracy of stress computation with this model depends on how well the semi-infinite geometry and homogeneity assumption are satisfied by the region of interest. Despite that this analytical model is not highly accurate, it can still improve the accuracy of the reconstructed Young' Modulus ratio by substituting the computed stresses into Eq. 2-11.

A more accurate approach to elastography uses an inversion algorithm to reconstruct the ratio of Young's Modulus of lesion to that of normal tissue. Several groups (Samani *et al,* Bishop *et al,* Skovorda *et al,* Kallel *et al*) have developed techniques to solve the elastography problem by inverting discretized Navier equations (Eq. 2-10).

The Navier equation (Eq. 2-10) is used in most inverse elastography methods. If the mechanical stimulation of the tissue ROI is static or quasi-static, the time dependent term will vanish and Eq. 2-10 reduces to:

$$\frac{E}{2(1-2\nu)(1+\nu)}u_{k,ki}+\frac{E}{2(1+\nu)}u_{i,kk}+\rho_0 b_i=0 \qquad \text{Eq. 2-13}$$

Since there are no analytical solutions for Eq. 2-13, this equation must be solved using Finite Element method described in section 3.3.2. For a stable solution of Eq. 2-13, a Poisson ratio of $\nu = 0.495$ is assigned for all soft tissues in the model. Displacements from Eq. 2-13 are computed using FEM. For elastic modulus reconstruction, one possible approach involves using a Gauss-Newton algorithm to solve the following least-squared error minimization problem:

$$min\|u_i^m(E_i)-u_i^m\|^2 \qquad \text{Eq. 2-14}$$

where $u_i^m(E_i)$ is the displacement field computed from the FEM model and u_i^m is the observed displacement field data. This minimization problem can be solved by updating the Young's Modulus of the finite elements in an iterative process.

2.3. Motion Estimation in US

Motion estimation in US is the procedure of estimating displacement or velocity vectors that describe the movement of each pixel in a US image or a sequence of US images. Having the displacements field at each time step in addition to a baseline image makes it

possible to reconstruct subsequent frames by warping the baseline image. An important application of tissue motion tracking is estimating soft tissue displacements resulting from mechanical stimulation. These displacements can be used for elastic modulus reconstruction in an elastography imaging framework. There are three main techniques for acquiring displacement data in Ultrasonic Elastography systems which are briefly described in the following sections.

2.3.1. Cross-Correlation Technique

Tissue displacements or velocities resulting from mechanical stimulation can be measured using one dimensional correlation. Correlation based techniques may be classified further as depending on internal or external source of mechanical excitation. The external source of mechanical excitation may be classified as static (quasi-static) or harmonic[36][37]. In quasi-static, mechanical stimulation is either static or with low frequency whereas in harmonic excitation, mechanical stimulation is applied with higher frequency than 40Hz.

This technique is based on finding maximum cross-correlation between two acquired A-line beams in pre- and post-compression images. Therefore it is only capable of obtaining displacement data in the axial direction with respect to US probe. Based on Eq. 2-11, the normal strain component in the axial direction can be obtained.

2.3.2. Visual Motion Inspection

Visual inspection of ultrasound B-mode images has been developed to study soft tissue motion characteristics, foetuses movements and growth of lesions. These techniques are based on acquiring displacement data using image processing techniques such as optical flow. They are capable of acquiring displacements in both lateral and axial directions. Therefore, it is possible to use Eq. 2-11 for estimating the strain components in the image plane. Having these strains may improve the accuracy of reconstructed ratio of Young's Modulus.

2.3.3. Doppler US Velocity Measurements

In harmonic Elastography techniques where the mechanical stimulation applied on the surface of the tissue is vibrational, tissue response is characterize by the velocity of each point in the tissue. Lubinski *et al* used tissue velocity induced by low vibration frequency excitation to determine the tissue's relative compressibility[15]. The basic idea behind Doppler US imaging is to exploit Doppler Effect to measure the velocity of the propagating wave. In harmonic elastography, Doppler velocity technique has been used to measure the wavelength of ultrasound wave travelling in different type of tissues.

2.4. Linear Viscoelastic Parameter Reconstruction in Harmonic Elastography

Viscoelasticity is the property of materials that display both viscous and elastic characteristics when undergoing deformation. Viscous materials, like honey, resist shear flow and strain linearly with time when a stress is applied. Pure elastic material stretches instantaneously when undergoing tension and return back to its original shape as quickly as before. Viscoelastic materials comprise both of these properties and, as such, exhibit strain function which varies with time. Each material to some degree has viscoelastic and elastic properties. While undergoing tension, it will display combination of elastic and viscoelastic behaviour. While elasticity is usually the result of tension or stretching along the direction of applied force or displacement boundary conditions, viscoelasticity is the result of diffusion of atoms or molecules inside the material.

Viscoelasticity is a molecular rearrangement. When viscoelastic material undergoes vibrational excitation, this molecular structure will move. This movement or rearrangement is called creep. Linear viscoelasticity models can be established by separating the creep response and load response. All linear viscoelastic models can be represented by the Volterra equation, which is based on establishing a function between stress and strain as follows:

$$\varepsilon(t) = \frac{\sigma(t)}{E_{inst,creep}} + \int_0^t K(t-t')\dot{\sigma}(t')dt' \qquad \text{Eq. 2-15}$$

where $E_{inst,creep}$ is the instantaneous elastic modulus for creep and $K(t)$ is the creep function. Linear viscoelasticity is usually applicable only for small deformations. There are a number of measurement devices that can be used in reconstructing viscoelastic parameters of materials. Broadband Viscoelastic Spectroscopy (BVS) and Resonant Ultrasound Spectroscopy (RUS) are commonly used to reconstruct viscoelastic parameter of the material[7].

2.5. Young's Modulus Reconstruction in Quasi-Static Elastography

In quasi-static elastography, mechanical stimulation is applied in low frequency fashion. Displacements data can be acquired using MR phase encoding or Ultrasonic motion estimation techniques. There are several research groups who have worked in the elastography field since the 1980s. Their approaches can be classified by the following three classes [22].

2.5.1. Strain Imaging

In earlier elastography techniques developed by Ophir *et al[*23] in the 1980s, displacement data was computed using pairs of A-lines acquired form specific points in the tissue ROI between pre- and post-compression images. In this case, displacement data was only computed in the axial direction. By assuming uniform distribution of stress throughout the ROI, one can use Eq. 2-12 to reconstruct the ratio of Young's Modulus of the tumour to that of normal tissue.

In this technique, strain images, usually referred to as elastograms, were constructed by finding the time shift between the pre- and post-compression images using cross-correlation function for each segment in the ROI. There are several methods of finding tissue displacements using cross-correlation, which are well-established in the literatures[37][38]. The generation of elastography imaging based on strain values involves computing time shifts using pair-wise cross-correlation between A-lines pairs acquired for pre- and post-compression images. A strain image is then created from a number of A-line pairs obtained with a specific amount of axial translation of the

transducer between pairs. In this technique, displacement lateral resolution is specified by many parameters such as frequency of emitted waves. One of the A-lines in each A-line pair is obtained while the transducer slightly compresses the tissue to have a full contact between the transducer and the specimen's surface. The compressed A-line, which is an A-line corresponding to the compressed tissue, is then acquired by compressing the specimen using transducer in axial direction as illustrated in Figure 2-5. The compressed A-line is shorter than the original A-line by $2\frac{dz}{c}$ where dz is the compression level and c is the speed of sound in the tissue. A-lines are obtained from various depths in the tissue ROI, and are divided into a number of overlapping segments obtained every one or two mm[36].

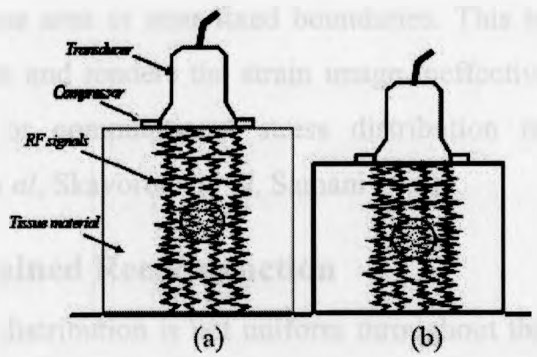

Figure 2-5: (a) Pre-compression Image (b) Post-compression Image after axially compression

Time scale and image acquisition are relative to the face of the transducer. As shown in Figure 2-5, the compression of an A-line becomes significant as we move towards the bottom of the specimen. In general, the time shift of the compressed A-line relative to the uncompressed A-line increases from 0 to maximum of $2\frac{dz}{c}$. Sometimes the time shift is either not observed or appears to be very small in some segments due to tissue heterogeneity.

Once time shifts, t_1 through t_N, assigned to each A-line pair are computed the corresponding strain distribution is computed by:

$$s_i = \frac{t_{i+1} - t_i}{2dz/_c} \; ; \quad i = 1 \; to \; N \qquad \text{Eq. 2-16}$$

where s_i is the strain estimation for segment i . The process of computing the strains using Eq. 2-16 is then repeated for all A-line pairs. Once the strain values for each segment in the FOV are computed, these values are assigned to a grey level in an image which varies from 0 to 255. For that purpose, a user can adjust a specific strain range to the grey levels in order to improve image contrast[36].

Since stress distribution in this technique is assumed to be uniform throughout the region of interest, the accuracy of reconstruction of the elastic Modulus ratio is not high. Strain images suffer from lack of accurate localization and extent determination of pathological tissue area. The reason is that in this technique stress concentration may occur in the boundary of stiff tissue area or near fixed boundaries. This issue invalidates the stress uniformity assumption and renders the strain image ineffective. Many researchers have exploited analytical or computational stress distribution models to overcome this shortcoming (Ophir *et al*, Skavoroda *et al*, Samani *et al*).

2.5.2. Unconstrained Reconstruction

In practice the stress distribution is not uniform throughout the region of interest due to many reasons including the finite size of the of the US probe used as tissue actuator. The stress is high near the actuator interface and reduces while moving away from the actuator. This phenomena is called hardening artefact [23]. Analytical models such as Boussinesq theorem can be used to find stress distribution throughout the ROI. This model assumes that the actuator size is finite while the tissue medium is homogeneous and semi-infinite. Analytical methods are appropriate for homogeneous media but they are not accurate for heterogeneous medium where different types of materials with different elastic moduli are present. To overcome this issue, reconstruction techniques must be formulated as inverse problems.

Skorovoda[30] proposed a method for tissue elasticity reconstruction by assuming that the tissue is incompressible linear elastic and isotropic but heterogeneous. Using some approximations, they converted the Navier equation to a system of equations. These

equations contain terms of functions of spatial derivatives of Young's modulus, the displacement field and the strain tensor. The displacement field as well as the Young's Modulus at points at the boundaries must be known for reconstruction. This method does not make any assumption such as elastic modulus piece-wise homogeneity, as such, it is referred to as unconstrained reconstruction technique. To limit the problem to 2 dimensions (2D), it is necessary to assume plane strain or plane stress models to reconstruct the tissue's Young's modulus with US imaging. In this technique, only the axial displacements were acquired And used for elasticity reconstruction [32].

Another method introduced by Sumi *et al* proposed an inverse problem, which assumes a plane stress state. This method leads to a linear system of equations for tissue elasticity reconstruction. In practice, several techniques have been developed to estimate displacements in the lateral direction using 2D cross-correlation, interpolation of axial components [37] or image processing techniques such as optical flow[10]. One of the techniques uses a mathematical constraint that describes tissue incompressibility to improve the estimation of lateral displacements from its axial component[15].

2.5.3. Constrained Reconstruction

As the inverse problem associated with unconstrained elastography reconstruction has shown to be highly ill-conditioned, some researchers have attempted to reduce the degree of this ill-conditioning by incorporating additional mathematical constraints. For instance, Samani *et al* [26] proposed a method where they assumed that each tissue type is homogeneous throughout its volume. This assumption simplifies the reconstruction algorithm by reducing the number of unknowns to be reconstructed. Furthermore, the reconstruction is much faster compared to unconstrained reconstruction methods. Constrained elastography techniques, like unconstrained techniques, do not use the uniform stress distribution assumption. As such, depending on the validity of the uniform elasticity distribution, the accuracy of the Young's Modulus reconstruction can be high. The techniques proposed by *et al* [26] involves segmenting images acquired by MRI to determine the tissue volumes where the elastic modulus distribution can be assumed as

uniform. The elasticity assigned to each region is then reconstructed iteratively or through an optimization process.

3. Theory and Methods

In this chapter theories used in the proposed methods will be described. First, techniques for displacement data acquisition will be introduced, followed by describing the theoretical approach used to compute stress distribution throughout a tissue ROI. Finally the reconstruction process will be described.

3.1. Optical Flow

The purpose of optical flow techniques is to estimate motion fields from sequences of images based on their spatiotemporal patterns of their image intensity (Lucas & Kanade 1981[16], Horn & Schunck 1981[8]). Several non-medical and medical applications use this technique to estimate motion fields, e.g. scene interpolation or motion tracking in biological tissues. To perform these tasks, a sufficiently accurate and dense 2D motion field is required. For applications such as consecutive frame construction, the error associated with the current method needs to be less than 10% (Barron et al. 1990, Jepson & Heeger 1990).

Several methods based on the concept of optical flow have been proposed [2]. One of the main shortcomings in optical flow techniques is lack of a quantitative method for evaluating different techniques using a single input with known results. Although there are major differences between each method, many of these methods comprise three main stages in computing a motion field:

- Pre-filtering with appropriate filters in order to smooth out the intensity value function.
- Computing basic parameters such as spatio-temporal derivatives in gradient based images.
- Solving proper equations. This often involves additional constraints to the basic optical flow equations, which vary from one method to another.

Brightness constancy is the most important principle used in optical flow techniques. This principle implies that image brightness corresponding to each point in the object of interest does not change as its position changes. In other words, each image

corresponding to an object represents a redistribution of the ensemble of pixel image intensities. This principle is described mathematically by the Brightness Constancy Equation (BCE). Optical Flow techniques are divided into four groups[2] based on their approach to solve the BCE:

- **Differential Techniques:** involves computation of optical flow using derivatives of the intensity function of the image or a filtered version of the image (using specific filters such as a Gaussian). Some researchers have used first order derivative (Horn & Schunck 1981, Nagel 1983) whereas some others used higher order derivatives of image intensity function.
- **Region-based Matching Techniques:** involves finding the best match leads to maximizing a similarity measure such as normalized cross-correlation or normalized mutual information or minimizing a distance measure such as the sum-of-squared differences (SSD).
- **Energy-based Methods:** in this technique, energy of output of some specific filters is used. This is done in Fourier domain.
- **Phase-based Techniques:** these techniques are defined in terms of the phase behaviour of band-pass filter outputs.

In this project, we have used a modified version of the Horn & Schunck technique and Lucas-Kanade method (differential techniqus) to estimate tissue displacements using pre- and post-compression images. The following sections will describe each technique in detail.

3.1.1. The 2D Motion Constraint Equation

Assume that a pixel located at (x, y, t) moves by δx, δy after time δt to $E(x + \delta x, y + \delta y, t + \delta t)$. Since $E(x, y, t)$ and $E(x + \delta x, y + \delta y, t + \delta t)$ are the image intensities of the same point, the brightness constancy principle dictates that they are identical, hence:

$$E(x + \delta x, y + \delta y, t + \delta t) = E(x, y, t) \qquad \text{Eq. 3-1}$$

This equation is the basic equation in each optical flow technique and is illustrated in Figure 3-1. Eq. 3-1 is called the Brightness Constancy Equation. This equation is valid

when small motions are involved. Therefore, it is possible to use Taylor series expansion at (x, y, t) in Eq. 3-1 to obtain:

$$E(x+\delta x, y+\delta y, t+\delta t) = E(x, y, t) + \frac{\partial E}{\partial x}\delta x + \frac{\partial E}{\partial y}\delta y + \frac{\partial E}{\partial t}\delta t + H.O.T \qquad \text{Eq. 3-2}$$

H.O.T is the Higher Order Terms which can be neglected since small motion between image frames is involved.

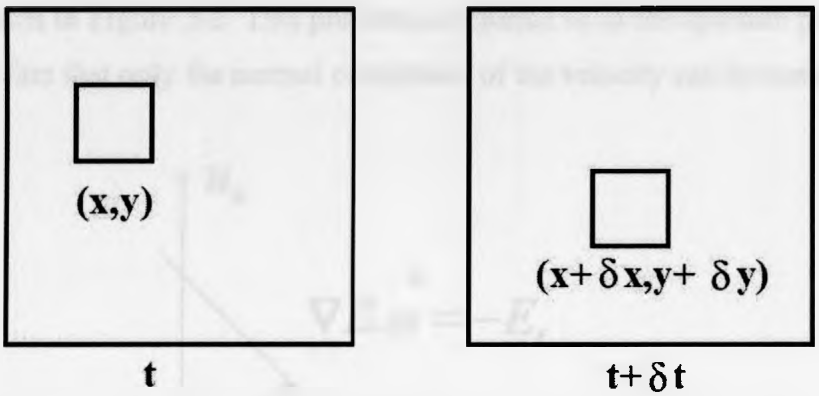

Figure 3-1: Image intensity at location (x, y, t) is the same as at location $(x+\delta x, y+\delta y, t+\delta t)$

As stated before, $E(x, y, t)$ and $E(x+\delta x, y+\delta y, t+\delta t)$ are image intensities of the same point and should be identical. Therefore, from Eq. 3-2 it follows that:

$$\frac{\partial E}{\partial x}\delta x + \frac{\partial E}{\partial y}\delta y + \frac{\partial E}{\partial t}\delta t = 0$$
$$\frac{\partial E}{\partial x}u_x + \frac{\partial E}{\partial y}u_y + \frac{\partial E}{\partial t} = 0 \qquad \text{Eq. 3-3}$$

Here $u_x = \frac{\delta x}{\delta t}$ and $u_y = \frac{\delta y}{\delta t}$ are the image velocities in x and y directions and $\frac{\delta E}{\delta x}$, $\frac{\partial E}{\partial y}$ and $\frac{\partial E}{\partial t}$ are image spatiotemporal derivatives at (x, y, t) , which can be re-written as follows:

$$E_x = \frac{\delta E}{\delta x}, E_y = \frac{\delta E}{\delta y} \text{ and } E_t = \frac{\delta E}{\delta t} \qquad \text{Eq. 3-4}$$

Therefore Eq. 3-3 can be re-written in the following form:

$$(E_x, E_y) . (u_x, u_y) = -E_t \qquad \text{Eq. 3-5}$$

or as:

$$\nabla E . \vec{u} = -E_t \qquad \text{Eq. 3-6}$$

where $\nabla E = (E_x, E_y)$ is the image intensity gradient and $\vec{u} = (u_x, u_y)$ is the velocity field or optical flow components at pixel located at (x, y) at time t. $\nabla E . \vec{u} = -E_t$ is called Brightness Constancy Equation, provides one equation for two unknowns (u_x,u_y). Eq. 3-6 is another representation of Brightness Constancy Equation. This can be represented by a line as shown in Figure 3-2. This problem is referred to as the aperture problem, which refers to the fact that only the normal component of the velocity can be computed [3].

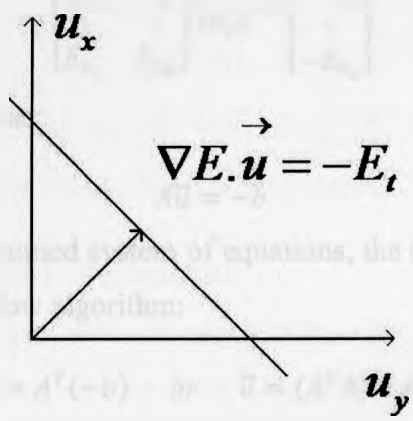

Figure 3-2: The Brightness Constancy Equation yields a line in $\vec{u} = (u_x, u_y)^T$ space.

3.1.2. Lucas-Kanade Algorithm

As was mentioned in the previous section, Brightness Constancy Equation, Eq. 3-6, has two unknown. To solve the Brightness Constancy Equation, another set of equations which are based on additional constraints are required. Many researchers such as Lucas & Kanade, Horn & Schunck, Nagel[21] have introduced additional constraint to Eq. 3-6. The additional constraint proposed by Lucas and Kanade [16] assumes that there are local constant flows in a neighbourhood. Based on this constraint, a non-iterative process was proposed by them to compute optical flow.

Assuming that the flow (u_x, u_y) is constant in a small window centered at pixel (x, y) of size m $*$ m with m > 1 which is centered at pixel and numbering pixels within the image as $1 \ldots n, n = m^2$, the following set of equations can be formed:

$$\begin{cases} E_{x_1}u_x + E_{y_1}u_y = -E_{t_1} \\ E_{x_2}u_x + E_{y_2}u_y = -E_{t_2} \\ \vdots \\ E_{x_n}u_x + E_{y_n}u_y = -E_{t_n} \end{cases} \qquad \text{Eq. 3-7}$$

With this there are more than two equations for the two unknowns (u_x, u_y), and therefore the system is over-determined. Hence, it follows that:

$$\begin{bmatrix} E_{x_1} & E_{y_1} \\ E_{x_2} & E_{y_2} \\ \vdots & \vdots \\ E_{x_n} & E_{y_n} \end{bmatrix} \begin{bmatrix} u_x \\ u_y \end{bmatrix} = \begin{bmatrix} -E_{t_1} \\ -E_{t_2} \\ \vdots \\ -E_{t_n} \end{bmatrix} \qquad \text{Eq. 3-8}$$

which can be re-written as:

$$A\vec{u} = -b \qquad \text{Eq. 3-9}$$

To solve the over-determined system of equations, the least square method is used in the Lucas-Kanade optical flow algorithm:

$$A^T A\vec{u} = A^T(-b) \quad or \quad \vec{u} = (A^T A)^{-1} A^T(-b) \qquad \text{Eq. 3-10}$$

or:

$$\begin{bmatrix} u_x \\ u_y \end{bmatrix} = \begin{bmatrix} \sum E_{x_i}^2 & \sum E_{x_i}E_{y_i} \\ \sum E_{x_i}E_{y_i} & \sum E_{y_i}^2 \end{bmatrix}^{-1} \begin{bmatrix} -\sum E_{x_i}E_{t_i} \\ -\sum E_{y_i}E_{t_i} \end{bmatrix} \qquad \text{Eq. 3-11}$$

with the summations going from $i = 1 \; to \; n$.

A weighted least square solution can be used to improve the accuracy of image velocity computation as shown in Eq. 3-6 applied to a constant value for $\vec{u}$ in each small spatial neighbourhood Ω:

$$\sum_{x,y \in \Omega} W^2(x,y)[\nabla E(x,y,t).\vec{u} + E_t(x,y,t)]^2 \qquad \text{Eq. 3-12}$$

where $W(x, y)$ denotes a window function that has more influence in the neighbourhood of the centre than points far from the centre. W coefficients are usually identical to Gaussian coefficients. The least-square solution to Eq. 3-12 is given by:

$$\vec{u} = (A^T W^2 A)^{-1} A^T W^2 (-b) \qquad \text{Eq. 3-13}$$

where for n pixels (for a $m * m$ neighbourhood, $n = m^2$), $(x_i, y_i) \in \Omega$ at a single time t:

$$\begin{aligned} A &= [\nabla E(x_1, y_1), \dots, \nabla E(x_n, y_n)] \\ W &= diag[W(x_1, y_1), \dots, W(x_n, y_n)] \\ b &= [E_t(x_1, y_1), \dots, E_t(x_n, y_n)] \end{aligned} \qquad \text{Eq. 3-14}$$

The solution to Eq. 3-12 can be solved using a closed form when $A^T W^2 A$ is a non-singular matrix. $A^T W^2 A$ is the following $2 * 2$ matrix:

$$A^T W^2 A = \begin{bmatrix} \sum W^2 E_{x_i}^2 & \sum W^2 E_{x_i} E_{y_i} \\ \sum W^2 E_{x_i} E_{y_i} & \sum W^2 E_{y_i}^2 \end{bmatrix} \qquad \text{Eq. 3-15}$$

Where the summations are taken over a neighbourhood of pixels located at (x, y) [1].

3.1.3. Horn-Schunck Technique

If every point in the image space is to move independently from adjacent points, there is a slight chance of recovering velocity field. This is the case when soft tissue deformation is involved where the movement of each point is affected by the movement of adjacent points. One way to impose an additional constraint to ensure motion continuity is minimizing the summation of flow gradient [7]:

$$\left(\frac{\partial u_x}{\partial x}\right)^2 + \left(\frac{\partial u_x}{\partial y}\right)^2 \quad \text{and} \quad \left(\frac{\partial u_y}{\partial x}\right)^2 + \left(\frac{\partial u_y}{\partial y}\right)^2 \qquad \text{Eq. 3-16}$$

Another method for introducing an additional constraint can be done by minimizing the Laplacian of each velocity component. The Laplacians of u_x and u_y are defined as:

$$\nabla^2 u_x = \frac{\partial^2 u_x}{\partial x^2} + \frac{\partial^2 u_x}{\partial y^2} \quad and \quad \nabla^2 u_y = \frac{\partial^2 u_y}{\partial x^2} + \frac{\partial^2 u_y}{\partial y^2} \qquad \text{Eq. 3-17}$$

Ideally, both Laplacians must be zero. Horn and Schunck [7] used the square of the velocity gradient magnitude as a smoothness measure representing an additional

constraint. This is in contrast with Lucas and Kanade's [16] algorithm that exploits the fact that optical flow is constant within a region in the image[2].

The algorithm that Horn-Schunck introduced leads to minimization of the sum of Brightness Constancy Equation errors:

$$\varepsilon_b = E_x u_x + E_y u_y + E_t \qquad \text{Eq. 3-18}$$

while minimizing the summation of spatial gradient of optical flow components as follows:

$$\varepsilon_c^2 = \left(\frac{\partial u_x}{\partial x}\right)^2 + \left(\frac{\partial u_x}{\partial y}\right)^2 + \left(\frac{\partial u_y}{\partial x}\right)^2 + \left(\frac{\partial u_y}{\partial y}\right)^2 \qquad \text{Eq. 3-19}$$

In practice, image intensity values contain errors due to interpolation and noise. As such one cannot expect ε_b to be exactly zero, therefore, using the Lagrange multiplier concept, the total error function to be minimized can be written as follow:

$$\varepsilon^2 = \iint (\varepsilon_b^2 + \alpha^2 \varepsilon_c^2)\, dx\, dy \qquad \text{Eq. 3-20}$$

It can be shown that minimizing the above leads to:

$$\begin{aligned} E_x^2 u_x + E_x E_y u_y &= \alpha^2 \nabla^2 u_x - E_x E_t \\ E_y^2 u_y + E_x E_y u_x &= \alpha^2 \nabla^2 u_y - E_y E_t \end{aligned} \qquad \text{Eq. 3-21}$$

Horn-Schunck suggested approximating Laplacians in Eq. 3-21 as follow:

$$\nabla^2 u_x \approx \kappa\left(\bar{u}_{x_{i,j,k}} - u_{x_{i,j,k}}\right) \quad \text{and} \quad \nabla^2 u_y \approx \kappa\left(\bar{u}_{y_{i,j,k}} - u_{y_{i,j,k}}\right) \qquad \text{Eq. 3-22}$$

where $u_{x_{i,j,k}}$ and $u_{y_{i,j,k}}$ denote the velocity in x and y directions at pixel location (i,j) at the kth frame, respectively. Also $\bar{u}_{x_{i,j,k}}$ and $\bar{u}_{y_{i,j,k}}$ denote local average of u_x and u_y at pixel location (i,j) at the kth frame, the respectively. In other words, $\bar{u}_{x_{i,j,k}}$ and $\bar{u}_{y_{i,j,k}}$ can be written based on the following matrix M_H:

$$M_H = \begin{bmatrix} \frac{1}{12} & \frac{1}{6} & \frac{1}{12} \\ \frac{1}{6} & 0 & \frac{1}{6} \\ \frac{1}{12} & \frac{1}{6} & \frac{1}{12} \end{bmatrix} \qquad \text{Eq. 3-23}$$

$$\bar{u}_{x_k} = u_{x_k} * M_H$$
$$\bar{u}_{y_k} = u_{y_k} * M_H$$

The κ factor is considered to be 3 provided that the local averages are computed using Eq. 3-23. Using the approximation to the Laplacians introduced in Eq. 3-22, Eq. 3-21 can be rewritten as follows:

$$\begin{aligned} (\alpha^2 + E_x^2)u_x + E_x E_y u_y &= \alpha^2 \bar{u}_x - E_x E_t \\ (\alpha^2 + E_y^2)u_y + E_x E_y u_x &= \alpha^2 \bar{u}_y - E_y E_t \end{aligned} \qquad \text{Eq. 3-24}$$

The determinant of the coefficients matrix equals $\alpha^2(\alpha^2 + E_x^2 + E_y^2)$. Solving for u_x and u_y leads to:

$$\begin{aligned} (\alpha^2 + E_x^2 + E_y^2)(u_x - \bar{u}_x) &= -E_x(E_x\bar{u}_x + E_y\bar{u}_y + E_t) \\ (\alpha^2 + E_x^2 + E_y^2)(u_y - \bar{u}_y) &= -E_y(E_x\bar{u}_x + E_y\bar{u}_y + E_t) \end{aligned} \qquad \text{Eq. 3-25}$$

Now there are two sets of equation to be solved. Horn and Schunck [7] suggested iterative techniques such as Gauss-Seidel to solve Eq. 3-28 by which a new set of velocity estimates (u_x^{n+1}, u_y^{n+1}) can be computed from the estimated derivatives and the average of the previous velocity estimate (u_x^n, u_y^n). The superscript n denotes the number of iterations:

$$\begin{aligned} u_x^{n+1} &= \bar{u}_x^n - \frac{E_x(E_x\bar{u}_x^n + E_y\bar{u}_y^n + E_t)}{\alpha^2 + E_x^2 + E_y^2} \\ u_y^{n+1} &= \bar{u}_y^n - \frac{E_y(E_x\bar{u}_x^n + E_y\bar{u}_y^n + E_t)}{\alpha^2 + E_x^2 + E_y^2} \end{aligned} \qquad \text{Eq. 3-26}$$

For approximating the intensity derivatives (E_x, E_y, E_t), the following convolution kernels have been used. This was originally proposed by Horn-Schunck and is based on finite difference calculus [14]:

$$M_x = \frac{1}{4}\begin{bmatrix} -1 & 1 \\ -1 & 1 \end{bmatrix}, \quad M_y = \frac{1}{4}\begin{bmatrix} 1 & 1 \\ -1 & -1 \end{bmatrix}, \quad M_t = \frac{1}{4}\begin{bmatrix} 1 & 1 \\ 1 & 1 \end{bmatrix} \qquad \text{Eq. 3-27}$$

Therefore, using these kernels in Eq. 3-27 intensity derivatives are computed as follows:

$$E_x = M_x * (E(k) + E(k+1))$$
$$E_y = M_y * (E(k) + E(k+1)) \qquad \text{Eq. 3-28}$$
$$E_t = M_t * (E(k+1) - E(k))$$

The original method proposed by Horn-Schunck [7] has some errors due to the fact that finite difference techniques are used to approximate spatiotemporal derivatives of image intensity. To reduce these errors, in this research the method was implemented with spatiotemporal pre-smoothing in conjunction with Sobel kernels to approximate the derivatives. Furthermore, images were pre-filtered using a Gaussian filter with a standard deviation of 1.5 pixels in space and 1.5 frames in time (1.5 pixels-frames) [18]. Also, a median filter was used to increase the signal-to-noise ratio as suggested in [39].

3.2. Hierarchical Framework for Optical Flow

Original methods proposed for optical flow are not capable of measuring large displacements as large as 10 pixels movement per frame. The reason for this lack of ability to estimate large motions is due to the fact that Taylor series expansion was used to form the Motion Constraint Equation Eq. 3-6. There, it was assumed that δx, δy and δt are small enough to allow using Taylor expansion. To address this shortcoming, Barron *et al* [3] proposed a hierarchical framework for computing optical flow involving relatively large motions gauged with pixel units.

The hierarchical framework of optical flow can be divided into four steps:

- Gaussian pyramid construction
- Image velocity (optical flow) calculation
- Image warping
- Coarse to fine refinements

This process must be repeated until the bottom of the pyramid is reached.

3.2.1. Gaussian Pyramid

To perform hierarchical framework of optical flow a multi-level representation of image is used. For this purpose, each image is blurred and down sampled to construct a coarser level of image. This blurring and down sampling slows the motion measured by pixel unit. Figure 3-3 illustrates the Gaussian pyramid representation.

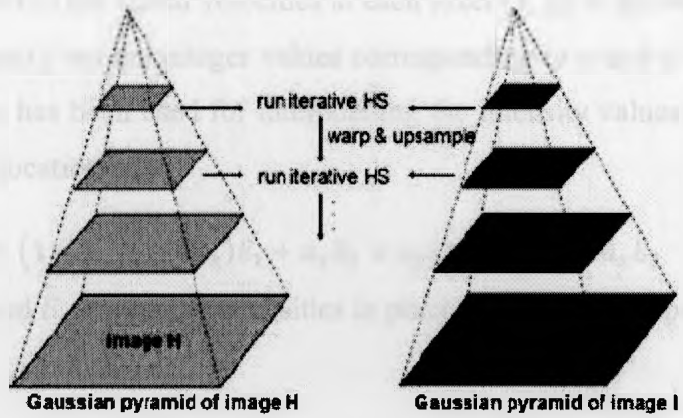

Figure 3-3: Gaussian pyramid representation of two images

Level 0 image is the baseline image. Level 1 image can be then constructed using level 0 image by blurring it using a Gaussian filter (with standard deviation of 1) and down sampling by factor 2 in dimensions. Level i is built from Level $i-1$ in a similar manner by further blurring and sub-sampling.

3.2.2. Image Velocity Calculation

The second step in hierarchical framework is to compute image velocity at each level, which can be carried out using a three-step process:

- Pre-smoothing the images to reduce noise and smooth out intensity distribution.
- Computing of intensity derivatives.
- Solving proper equations (based on the method).

Methods used in this project were described in sections 3.1.2 and 3.1.3.

3.2.3. Image Warping

The third step in the hierarchical technique framework is image warping based on velocity vectors calculated in the previous step. The image velocity parametric model (Horn-Schunck) introduced in the previous section is sufficiently accurate for small motions; however, for cases involving large motions, images have to be warped iteratively throughout the hierarchical process. Image warping is performed by using a

computed flow field as the initial velocities at each pixel (x, y) in the sequence. For pixel location (x, y), i and j are the integer values corresponding to x and y, respectively. The following equation has been used for interpolating the intensity values to reconstruct the image intensity at location(x, y).

$$E(x, y) = (1 - u_y)(1 - u_x)E_1 + u_x E_2 + u_y(1 - u_x)E_4 + u_x E_3 \qquad \text{Eq. 3-29}$$

where E_1, E_2, E_3 and E_4 are image intensities in pixels adjacent to the pixel located at (i, j).

3.2.4. Coarse to Fine Refinement

The final step in hierarchical framework of optical flow is coarse to fine refinements, which involves the following steps:

- Computing velocities at root level
- Projecting each computed velocity (after doubling it)
- Warping image to remove the effect of velocities in upper Levels.

This process is continued until the top of pyramid is reached where Level 0 images are located.

3.3. RF Data Cross-Correlation Techniques for Motion Estimation

As mentioned earlier, strain can be estimated from ultrasonic wave form using cross-correlation. As a result of applying compression to the tissue, a time shift is observed. The wave form shifts by a small amount, which can be determined by correlation. Displacement values are then computed using estimated time shifts provided that the velocity of sound within the tissue is approximately constant.

The peak of cross-correlation function corresponds to the required time shift. Figure 3-4(a) depicts an A-line pair while Figure 3-4(b) illustrates normalized cross-correlation between two signals.

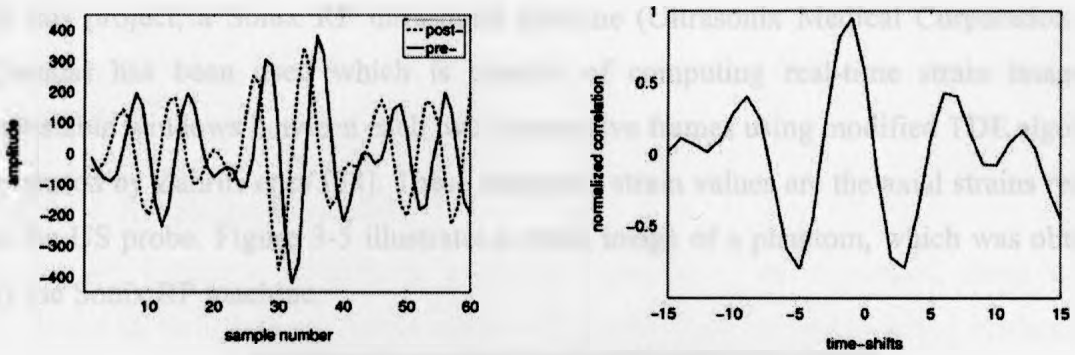

Figure 3-4: (a) An A-line pair (b) Cross-correlation between two A-lines

Several methods to estimate the peak of cross-correlation functions have been proposed. There are basically two main techniques. One is to fit, for example, a parabola or a cosine, etc. to the actual digitized samples. While this technique works well and it is easy to implement it produces large biases. Another technique involves filtering the spectrum using a boxcar-type filter, which is the same as performing convolution in the time domain with a sinc function. This process creates many new samples in between the original samples (up-sampling), which allows approximating the peak location very accurately. Having found the peak, one can compute the displacement by incorporating the average velocity of ultrasonic wave in soft tissues, which is accepted to be 1540 m/s [17].

The properties of Time Domain Cross-correlation (TDE) are well established in the literature [37] and it is easy to implement. TDE cannot be used in real-time applications where real-time estimation of motion field is necessary since TDE is computationally demanding. The reason for being computational demanding is that searching over a large area makes the algorithm slow [38]. Another drawback of the original TDE is that it may produce false-peaks that introduce errors in time shift estimations. Zahriri *et al* [38] proposed a technique based on the original TDE algorithm which exploits the fact that in an RF frame, adjacent points in a window correspond to tissue regions that are close to each other. Their method is similar to TDE but it incorporates information about displacements of adjacent points to have a rough prediction of displacements of the desired points and, hence it reduces the searching interval [37].

In this project, a Sonix RP ultrasound machine (Ultrasonix Medical Corporation, BC, Canada) has been used which is capable of computing real-time strain images in adjustable windows between each two consecutive frames using modified TDE algorithm proposed by Zahriri *et al* [38]. These computed strain values are the axial strains relative to the US probe. Figure 3-5 illustrates a strain image of a phantom, which was obtained by the Sonix RP machine.

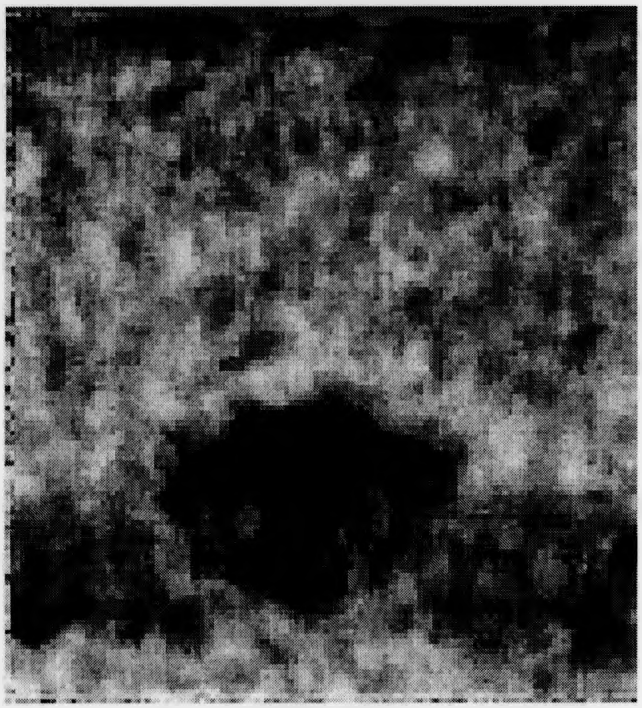

Figure 3-5: Strain image acquired by Sonix RP machine

3.4. Stress Distribution Calculation Methods

As mentioned earlier, Eq. 2-11 has been used for reconstructing the ratio of Young's modulus of the normal tissue to that of the suspicious area. Stress distribution in the heterogeneous medium may be assumed as uniform. With such assumption, the ratio is simply calculated using Eq. 2-12, which is the reciprocal of the ratio of strain values in each point. However, as noted earlier, the stress uniformity is not accurate since stress concentration may occur near the boundary of stiffer areas. Hence, the needs for incorporating accurate stress distribution information in the reconstruction process.

Several analytical and numerical methods for stress distribution have been introduced based on the theory of elasticity. Some of these methods will be described in following sections.

3.4.1. Analytical Models

When two bodies with different mechanical properties are in contact, stress will be produced in both bodies. Stress components were first computed using mathematical models proposed by Hertz in 1881[42]. One of the useful tests used to find material properties is the indentation test, which is used extensively in mechanical engineering applications. This has motivated researchers to formulate this test using mathematical models for decades. One of the models of computing stress components resulting from indentation was proposed by Boussinesq in 1885[42]. Boussinesq proposed a solution for a point load applied on the surface of a semi-infinite medium. For any arbitrary load distribution, the superposition principle can be applied to find resultant stress components.

The stresses within a solid loaded by a point contact were calculated by Boussinesq and are given in polar coordinates in following equations:

$$\sigma_r = \frac{P}{2\pi}\left[(1-2\nu)\left[\frac{1}{r^2} - \frac{z}{r^2(r^2+z^2)^{\frac{1}{2}}}\right] - \frac{3r^2 z}{(r^2+z^2)^{\frac{5}{2}}}\right]$$

$$\sigma_\theta = \frac{P}{2\pi}(1-2\nu)\left[-\frac{1}{r^2} + \frac{z}{r^2(r^2+z^2)^{\frac{1}{2}}} + \frac{z}{(r^2+z^2)^{\frac{3}{2}}}\right] \qquad \text{Eq. 3-30}$$

$$\sigma_z = -\frac{3P}{2\pi}\frac{z^3}{(r^2+z^2)^{\frac{5}{2}}}$$

$$\tau_{rz} = -\frac{3P}{2\pi}\frac{rz^2}{(r^2+z^2)^{\frac{5}{2}}}$$

Except at the origin, the surface stresses $\sigma_z, \tau_{yz}, \tau_{zx} = 0$. Figure 3-6 illustrates the point load applied to a semi-infinite medium.

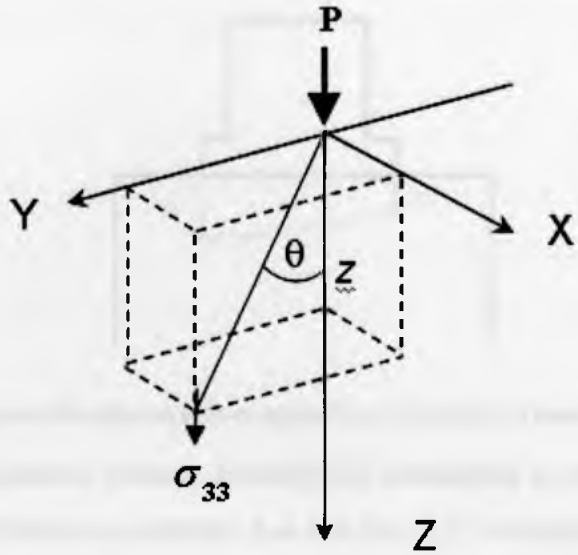

Figure 3-6: point load applied to a semi-infinite medium

In the Boussinesq solution, the material is assumed to be homogeneous and semi-infinite. This is not a valid assumption when the region of interest, e.g. tissue, has a finite size and includes a suspicious area. In this case, the material in heterogeneous and stresses computed using Eq. 3-30 is no longer valid. To address this issue, in this research initially a solution based on micromechanics theorem was incorporated to improve the Young's modulus reconstruction accuracy. Micromechanics theory is a theory based on continuum mechanics which deals with computation of stress and strain field in materials that contain inclusions. Biological tissues with cancerous tumours can be considered as homogeneous elastic materials containing a harder/softer inclusion [13]. In this research, it was assumed that both the tumour and normal tissues are isotropic with different Young's moduli. Moreover, when a force is applied by a US probe, a distribution of point load on the surface of the tissue will be formed. As mentioned earlier, the superposition principle is used here to find stresses resulting from the probe's distributed load.

In reality, the size of the probe is considerably smaller than the tissue size. This justifies assuming a linear load distribution on the surface underneath the probe as shown in Figure 3-7. F_1 and F_2 in this figure indicate forces measured by two load cells attached to the US probe as described in Chapter 4.

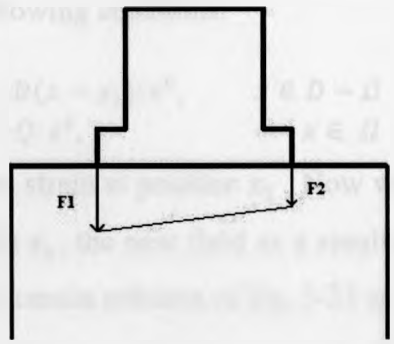

Figure 3-7: Linear distribution of load applied by a US probe to a tissue mimicking phantom

Based on a micromechanics theory, Eshelby[13] developed a system of equations to investigate strain distribution in material. Lui and Sun [13] developed an analytical model based on Eshelby's method to investigate the influence of tumour embedded in a normal tissue on strain distribution. According to this model, if the position, the size of tumour and its elastic property are known, the strain field can be computed for the whole tissue (e.g. breast) using the micromechanics theory. Total strain distribution in the tissue model can be determined by the following equation:

$$\varepsilon(x) = \varepsilon^0(x) + \varepsilon^d(x) \qquad \text{Eq. 3-31}$$

where $\varepsilon^0(x)$ is the homogenous strain field due to far-field stress σ^0 on the matrix without the inclusion and $\varepsilon^d(x)$ is the strain filed due to presence of tumour. Figure 3-8 illustrates the domain including the lesion area:

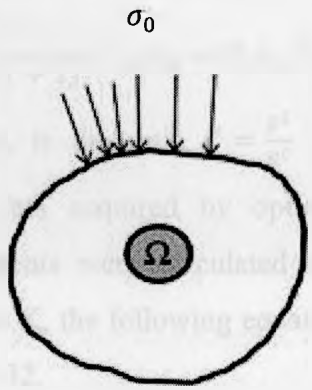

Figure 3-8: Domain with inclusion undergoing pressure σ_0

For a specific lesion centered in x_1 and incompressible tissue matrix ($\nu = 0.5$) , $\varepsilon^d(x)$ can be calculated using the following equations:

$$\varepsilon^d(x) = \begin{cases} -B(x - x_1): \varepsilon^0, & x \in D - \Omega \\ -Q: \varepsilon^0, & x \in \Omega \end{cases} \qquad \text{Eq. 3-32}$$

Assume that $\varepsilon^e(x_1)$ is the local strain at position x_1 . Now with a homogeneous inclusion added with its centre located at x_1, the new field as a result of this inclusion, $\varepsilon^d(x)$, can be estimated from the infinite domain solution of Eq. 3-35 as follows:

$$\varepsilon^d(x) = \begin{cases} -B(x - x_1): \varepsilon^e(x_1), & x \in D - \Omega \\ -Q: \varepsilon^e(x_1), & x \in \Omega \end{cases} \qquad \text{Eq. 3-33}$$

Accordingly, the total strain distribution in the tissue with inclusion should be summed as follows:

$$\varepsilon(x) = \begin{cases} \varepsilon^e(x) - B(x - x_1): \varepsilon^e(x_1), & x \in D - \Omega \\ \varepsilon^e(x) - Q: \varepsilon^e(x_1), & x \in \Omega \end{cases} \qquad \text{Eq. 3-34}$$

where B and Q are four-rank coefficient tensors that can be determined using the following equations:

$$\begin{aligned} B_{\alpha\beta\gamma\tau}(x - x_1) = \frac{(K-1)}{2(K+1)}\rho^2 \Big[& 8\,(-2 + 3\rho^2) n_\alpha n_\beta n_\gamma n_\delta \\ & + 2(1 - 2\rho^2)(\delta_{\alpha\gamma} n_\beta n_\tau + \delta_{\alpha\tau} n_\beta n_\gamma + \delta_{\beta\gamma} n_\alpha n_\tau + \delta_{\beta\tau} n_\alpha n_\gamma) \\ & + 4(1 - 2\rho^2)\delta_{\alpha\beta} n_\gamma n_\tau + 2\left(1 - 2\rho^2 - \frac{1}{K}\right)\delta_{\gamma\tau} n_\alpha n_\beta \\ & + \left(\rho^2 - 1 + \frac{1}{K}\right)\delta_{\alpha\beta}\delta_{\gamma\tau} + \rho^2(\delta_{\alpha\gamma}\delta_{\beta\tau} + \delta_{\alpha\tau}\delta_{\beta\gamma})\Big] \\ Q_{\alpha\beta\gamma\tau} = \frac{(K-1)}{2K(K+1)} & \left[\delta_{\alpha\beta}\delta_{\gamma\tau} + K(\delta_{\alpha\gamma}\delta_{\beta\tau} + \delta_{\alpha\tau}\delta_{\beta\gamma})\right] \end{aligned} \qquad \text{Eq. 3-35}$$

where K, the modulus contrast, is the ratio $K = \frac{E^1}{E^0}$. In this project, strain values computed from displacement data acquired by optical flow was used as $\varepsilon^d(x)$. Furthermore, the stress components were calculated using Eq. 3-35 and $K = 1$ was incorporated. Finally, to calculate K, the following equation was used to calculate $\varepsilon^0(x)$, followed by substitution in Eq. 3-32.

$$\varepsilon_r = \frac{\sigma_r - \nu(\sigma_\theta + \sigma_z)}{E}$$
$$\varepsilon_\theta = \frac{\sigma_\theta - \nu(\sigma_r + \sigma_z)}{E} \qquad \text{Eq. 3-37}$$

3.4.2. Finite Element Method

Another method for computing stress distribution is Finite Element Method (FEM).FEM is a numerical technique for finding approximate solutions of partial differential equations (PDE) as well as of integral equations. In elasticity analysis, FE model converts partial differential equation to a system of linear equations that can be solved numerically. When solving a deformable body problem using FEM, the body is first discretized into a group of homogeneous elements which has a number of nodes (depending on elements type) where the displacements will be defined. This discretization process is referred to as FE meshing and the resulting discretized domain is called an FE mesh. Figure 3-9 shows mesh generated using a schematic diagram of a numerical breast phantom. The displacements within each element are computed using interpolation of nodal displacements.

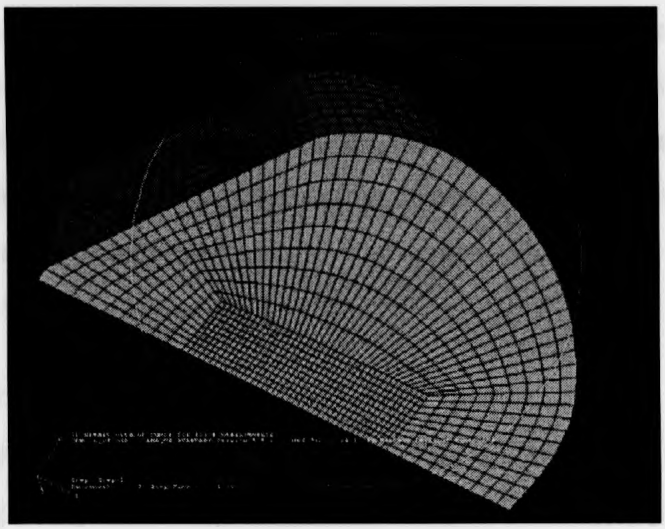

Figure 3-9: FE mesh for a numerical breast phantom

Using an approximation, the governing equations of elastic deformation are converted to a small set of linear equations for each element called element stiffness matrix. These

equations presented in matrix form are then assembled into a global stiffness matrix $\boldsymbol{K}$. The global stiffness matrix is related to the displacements as follows:

$$\boldsymbol{K}u = f \qquad \text{Eq. 3-38}$$

where u is the unknown displacement vector and f is the force vector. The unknown displacement vector u contains all the nodal displacements the finite elements and f is the force acting on each node. One can solve for u after applying the boundary conditions to Eq. 3-38 for known nodal forces and inverting the global stiffness matrix $\boldsymbol{K}$. Many commercial software packages such as ABAQUS (Dassault Systèmes Simulia Corp.) are available for performing this analysis. The accuracy of the FE analysis depends on several factors such as the type of the chosen elements, their quality and density. Strategies for generating FE meshes are discussed in Appendix A.

Having solved Eq. 3-41 for unknown u, strain values can be computed, and by having estimation of Young's modulus of each element, stresses can be calculated easily. FEM is known to be computationally expensive. Depending on the number of elements in the discretized domain, it requires massive amount of calculation to compute the displacements. Elastography techniques based on FEM involve iterative processes to update the value of Young' Modulus by minimizing specific measures such as least squares errors between actual reaction forces [27] or normalized mutual information [20], etc. Although FEM is known to be accurate in elastic analysis, it is not suitable for real-time applications because it is computation time demanding. As an alternative technique that is suitable for real-time applications, a statistical FE method developed in our laboratory was used.

3.4.3. Statistical Model

As stated in the previous section, although FE analysis is known to be accurate enough, it suffers from being computationally time demanding. The time required for solving a system of linear equations is proportional to the number of elements in the discretized domain as well as complexity of contact boundary conditions. Hence, conventional FEM cannot be exploited in real-time applications such as US elastography. To address this

issue, a novel technique has been developed in our research group by Khalaji *et al* (ref) where they incorporated pre-processed data obtained from FE analysis of a large number of similar objects in a statistical shape model framework.

The basic idea behind the statistical shape models is that there is a high degree of similarity between specific organs such as the prostate or breast. Therefore, each shape of an organ can be expressed mathematically in terms of the mean shape of the organ set (for N shapes) and eigenvectors representing the organ's shape modes. The following equation shows how a new shape of an organ that belongs to a particular class of organs (e.g. breast) can be expressed:

$$\boldsymbol{x} = \bar{\boldsymbol{x}} + \boldsymbol{P}\boldsymbol{b} \qquad \text{Eq. 3-39}$$

where $\boldsymbol{P} = (\boldsymbol{p_1}, \boldsymbol{p_2}, \dots, \boldsymbol{p_t})$ is the matrix of the first t eigenvectors calculated using Principal Component Analysis (PCA), $\boldsymbol{b} = (b_1, b_2, \dots, b_t)^T$ is a weights vector and $\bar{\boldsymbol{x}}$, the mean shape, is calculated using the following equation:

$$\bar{\boldsymbol{x}} = \frac{1}{N}\sum_{i=1}^{N} \boldsymbol{x_i} \qquad \text{Eq. 3-40}$$

where $\boldsymbol{x_i}$ is defined a set of discrete points representing the shape's outline as follows:

$$\boldsymbol{x_i} = (x_{i0}, y_{i0}, x_{i1}, y_{i1}, \dots, x_{ik}, y_{ik}, \dots, x_{in-1}, y_{in-1})^T \qquad \text{Eq. 3-41}$$

In the proposed technique, the same concept is used to find the FE analysis results. The basic idea is that for the same class of objects and the same boundary conditions and loading, only the geometry of organ of interest is sufficient to predict the FE model results. Similar to Eq. 3-42, the FE results, e.g stress field, can be expressed as follows:

$$\boldsymbol{\sigma} = \bar{\boldsymbol{\sigma}} + \boldsymbol{Q}\boldsymbol{c} \qquad \text{Eq. 3-42}$$

where $\bar{\boldsymbol{\sigma}}$ is the mean stress field obtained from FE analysis of all training shape data undergoing a specific loading and boundary conditions. Also $\boldsymbol{Q} = (\boldsymbol{q_1}, \boldsymbol{q_2}, \dots, \boldsymbol{q_s})$ is the matrix of the first s eigenvectors of the stress field covariance matrix and $\boldsymbol{c} = (c_1, c_2, \dots, c_s)^T$ is a weights vector. To be able to calculate the stress field of a similar organ not included in the data set, a pre-processing training step is required. This step involves finding $\bar{\boldsymbol{x}}, \boldsymbol{P}, \boldsymbol{b}$ and $\bar{\boldsymbol{\sigma}}, \boldsymbol{Q}, \boldsymbol{c}$ for each shape in the training data set. Once they have

been computed, a Multilayer Feed Forward Neural Network (FF-NN) is trained to establish a relationship between vectors $\boldsymbol{b}$ and $\boldsymbol{c}$. For a new shape which may not be in the training data set, first vector $\boldsymbol{b}$ is calculated using Eq. 3-42, which then fed into the trained Neural Network to obtain $\boldsymbol{c}$. The latter is used to find $\boldsymbol{\sigma}$ using Eq. 3-42.

The original method proposed by Khalaji *et al*[12] involved predicting the nodal displacements when an organ undergoes specific amount of displacement loading on the boundary. Based on the theory of elasticity, it was realized that Statistical Finite Element Method (SFEM) can be exploited to predict the stress distribution in each shape of the training data set. The basic idea behind this approach is that when the amount of loading on the surface of a homogeneous tissue and the tissue geometry itself are known, the stress field can be predicted irrespective of the tissue's Young's modulus. In other words, the stress fields remain consistent for different tissue Young's modulus values. Figure 3-10 illustrates the fact that two different media with consistent geometry and the force boundary conditions but with different Young's Modula, the σ_{11} stresses are identical in both cases.

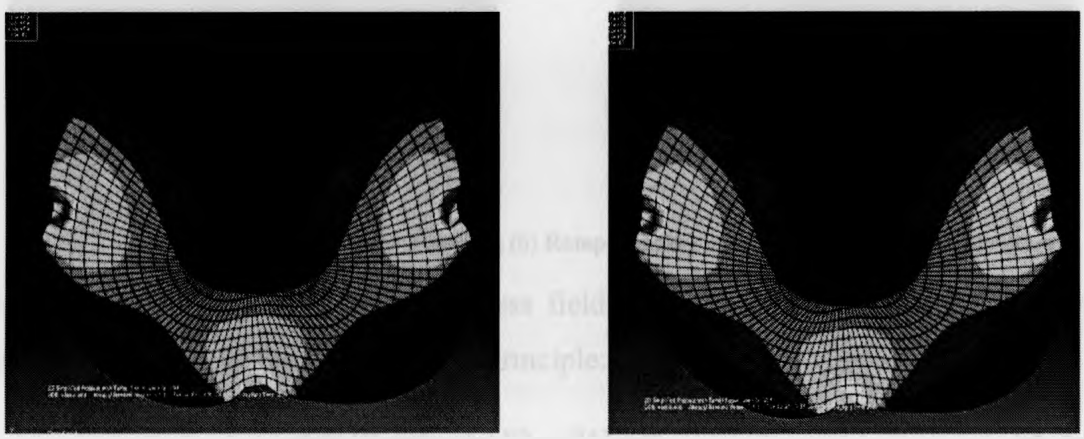

(a) **(b)**

Figure 3-10 : σ_{11} stress for tissue with YM of (a) 5kPa (b) 15kPa

For modeling US elastography loading, two main modes of force loading applied on the surface have been assumed. For any arbitrary combination of $F1$ and $F2$, shown in Figure 3-7, one can predict the stress distribution using linear combination of these two main modes. The first main mode involves applying a uniformly distributed load equals to 1gr

on the surface of the FE model and computing corresponding stress field as shown in Figure 3-11(a). The second main mode involves applying a ramp distributed load, increase linearly for, 0 to 1gr, on the surface of the FE model and calculating corresponding stress field as shown in Figure 3-11(b). Therefore, two different NNs associated with each main mode were trained. The first NN computes the stress field resulting from uniform loading while the second calculates the stress field induced by the ramp loading. 300 FE models with random breast like geometry with different randomly generated Young's modulus values of background and tumour (within specific range) were generated. Each one of these models underwent uniform and ramp loadings. Furthermore, the tumour location as well as its geometry was varied while generating the training data set.

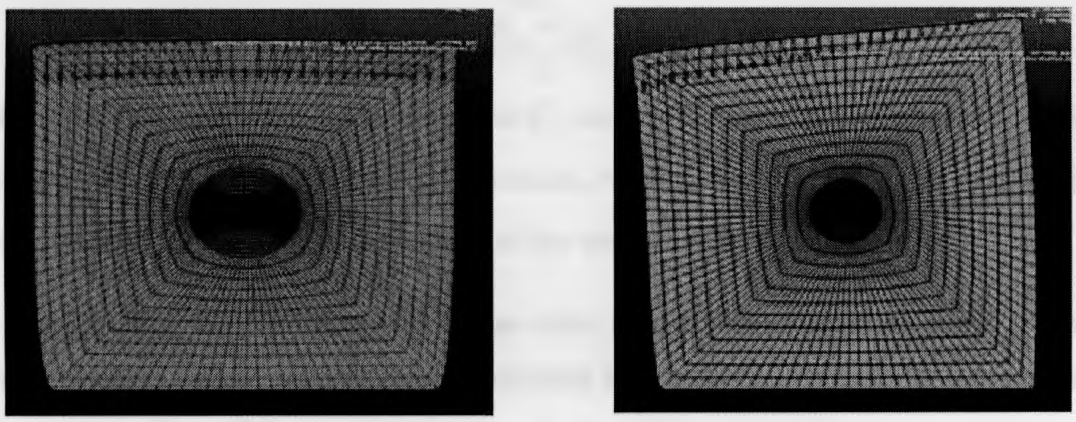

(a) (b)

Figure 3-11 : (a) Uniform loading (b) Ramp Loading applied on a block shape phantom

For measured values of $F1$ and $F2$, stress field can be computed using the following equation according to the superposition principle:

$$\boldsymbol{\sigma} = F1 * \boldsymbol{\sigma}_{ul} + (F2 - F1) * \boldsymbol{\sigma}_{rl} \qquad \text{Eq. 3-43}$$

where $\boldsymbol{\sigma}_{ul}$ and $\boldsymbol{\sigma}_{rl}$ represent the stress fields computed from uniform loading mode and ramp loading modes, respectively. Note that in all of the FE analysis conducted in the phantom studies of this research, the plane strain model was used where out of plane strains are equal to 0. This assumption helps simplifying the strain tensor calculations since out of plane displacements cannot be estimated using 2D pre- and post-compression images.

For a new FE model associated with a new shape of the organ of interest, the geometry of suspicious area as well as loading on the boundary of the organ and the ratio of Young's modulus of normal tissue to that of the suspicious lesion is fed into the NNs to compute the corresponding stress field.

3.5. Young's Modulus Reconstruction

Once the stress field is computed with either analytical or numerical models, the measured strain field can be used to reconstruct Young's modulus using Hooke's law as follows:

$$E_{x_i} = \frac{\sigma_{xx_i} - \nu\sigma_{yy_i}}{\varepsilon_{xx_i}}$$
$$E_{y_i} = \frac{\sigma_{yy_i} - \nu\sigma_{xx_i}}{\varepsilon_{yy_i}} \qquad \text{Eq. 3-44}$$
$$E_{recon_i} = \frac{E_{x_i} + E_{y_i}}{2}$$

Where i denotes element number, E_{x_i} and E_{y_i} are the Young's modulus values obtained from the measured strains in x and y directions, respectively, and E_{recon_i} is their average value, which is a more accurate estimate of the element's Young's modulus.

In this research, two different approaches were used for reconstructing tissue Young's modulus where different methods for computing the strain and stress fields were applied. These approaches will be described in detail in the following sections.

3.5.1. First Approach

In the first approach, optical flow was used to estimate the strain distribution from pre- and post-compression US images. To reconstruct Young's modulus in a tissue mimicking phantom, two different methods using optical flow were employed. One method involved using Boussinesq theory in conjunction with Hooke's law to determine Young's modulus values. This method assumes that Young's modulus values of both the normal and tumour tissues are unknown. A major drawback in this method is that it does not take into account the presence of the inclusion in its stress estimation. The other method involved using the micromechanics theory discussed in Section 3.4.1 to address the stress calculation issue in the former method. The formalism of this technique leads to an

optimization problem as will be described later. For both techniques, it was assumed that the domain, as illustrated in Figure 19-3, is infinite in comparison with the applied forces on the surface. While Young's modulus value of the normal tissue was assumed to be unknown in the first method, in the second method the normal tissue's Young's modulus was assumed to be known based on values reported in the literature (Samani *et al* [3]). $\varepsilon(x)$ was estimated using the optical flow techniques described in previous sections. As stated before, the second method involves calculating the stress field using Boussinesq theory. This was done by inputting a Young's modulus value of 3.25 kPa corresponding to normal breast tissue in the analytical model. With these stresses, the strain field of the homogeneous material ($\varepsilon^e(x)$) was calculated. By combining Eq. 3-34 to 3-38 and substituting the calculated values of $\varepsilon^e(x)$ and the $\varepsilon(x)$ estimated from the optical flow techniques, a system of nonlinear equations with K as the unknown parameter was obtained. To determine K, a Golden Section Search (GSS) optimization was used. The summary of the procedure used to estimate K is given in the flowchart depicted in Figure 3-12.

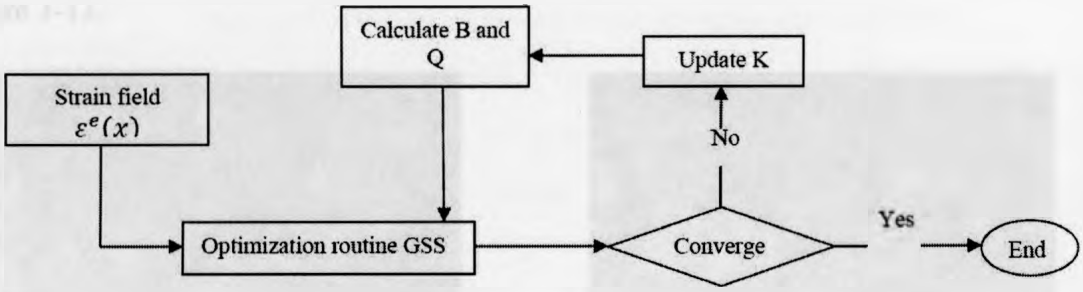

Figure 3-12 : Flowchart of updating K

In this approach the absolute Young's modulus values of normal tissue and lesion have been reconstructed.

3.5.2. Second Approach

In this approach RF signal cross correlation technique and SFEM were employed to estimate the strain and stress field, respectively. While the optical flow technique is

capable of estimating displacements in axial and lateral directions, it suffers from lack of sufficient accuracy. As stated earlier, strain tensors are obtained by differentiating the estimated displacement values. It is known that differentiation amplifies errors due to displacement errors associated with the optical flow technique. Therefore, as alternative, axial strains were obtained using RF signal cross-correlation techniques. The Sonix RP US machine has incorporated a cross correlation technique to provide strain values with adjustable windows for the ROI. While motion estimation using cross-correlation techniques provide axial displacements only, they are known to be the most accurate techniques for motion estimation in US elastography applications. Figure 3-13(a) illustrates a strain image obtained using the Sonix RP machine. For stress field estimation, the tissue geometry including the suspicious area needs to be fed into a NN as described earlier. To obtain the lesion geometry in the tissue mimicking phantom study, strain image was used. Having the tissue strain image, a Discrete Dynamic Contour (DDC) segmentation technique[41] was used to automatically segment and estimate the geometry of the suspicious area. In the DDC process, first a rough outline of the suspicious area (shown by lower intensity values) was manually drawn. DDC, thus, iteratively modifies this outline until it converges to area good quality outline as shown in Figure 3-13.

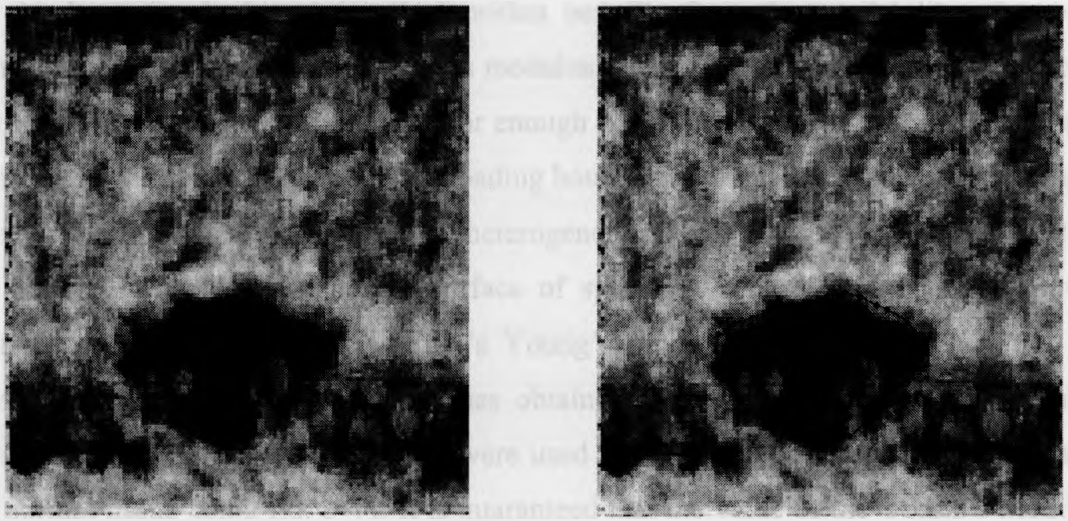

(a) (b)

Figure 3-13 : (a) Strain image provided by Sonix RP machine (b) Segmented to find the boundary of the suspicious area

Once the geometry of suspicious area is found, stress distribution calculation is calculated using SFEM. Since the ratio of Young's Modulus of the lesion to that of the normal tissue is unknown, an initial guess of this ratio was computed using Eq. 2-12. An iterative process was then carried out to update the ratio of Young's Modulus as shown in Figure 3-14. In each iteration, a new value for the ratio is computed and then fed into the NN for updating the stress field.

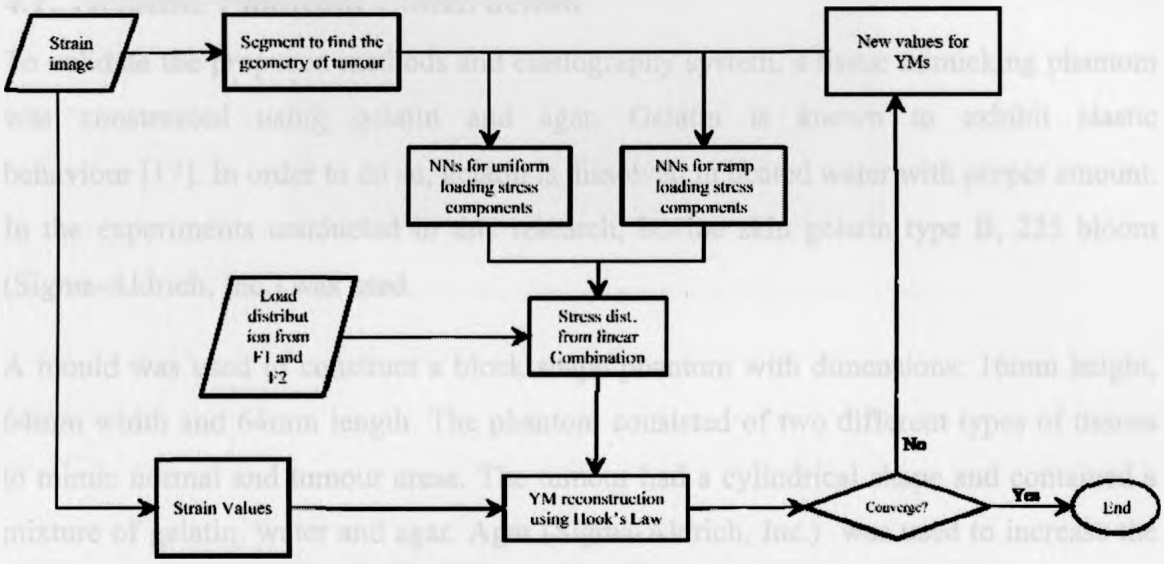

Figure 3-14 : Flowchart of iterative process of elastography reconstruction

As can be noticed, the proposed algorithm benefits from the availability of a good estimate of the normal tissue's Young's modulus. Based on FE analysis, it can be shown that if the tumour is located deep and far enough from the loading boundary, the stress in elements located right underneath the loading boundary is almost the same irrespective of whether the tissue is homogeneous or heterogeneous. Note that as was stated in section 3.4.3, if the force loading on the surface of specimen and its geometry are known, regardless of the homogeneous tissue's Young's modulus value, the stress fields are identical. Therefore, actual strain values obtained from strain imaging and the stress distribution in homogeneous material were used to reconstruct the Young's Modulus of the normal tissue using Eq. 3-44. It is guaranteed that the value of the Young's Modulus computed using Eq. 3-44 is a good estimate of the normal tissue's Young's Modulus value (based on theory of elasticity).

4. Experimental Methods

In this chapter methods used in this research's tissue mimicking phantom studies will be described. This chapter comprises the construction of gelatine phantom, description of the force data acquisition system used in the proposed elastography system and an indentation apparatus used for independent measurement of tissue elasticity.

4.1. Gelatine Phantom Construction

To validate the proposed methods and elastography system, a tissue mimicking phantom was constructed using gelatin and agar. Gelatin is known to exhibit elastic behaviour [17]. In order to do so, gelatin is dissolved in heated water with proper amount. In the experiments conducted in this research, bovine skin gelatin type B, 225 bloom (Sigma-Aldrich, Inc.) was used.

A mould was used to construct a block shape phantom with dimensions: 16mm height, 64mm width and 64mm length. The phantom consisted of two different types of tissues to mimic normal and tumour areas. The tumour had a cylindrical shape and contained a mixture of gelatin, water and agar. Agar (Sigma-Aldrich, Inc.) was used to increase the stiffness of the tumour in comparison to the normal tissue mimicking gelatin. Furthermore, glycerol was used, which regulates the sound speed in both normal and tumour areas to be consistent with the speed of 1540m/s [17]. Also, Sigmacel was added to introduce backscattering effect to the tissues. Different amounts of sigmacel were used in the gelatine and agar to slightly vary the backscattering effect in order to have proper US image contrast. Table 4-1 shows the amount of different materials that was used to construct the tissue mimicking phantom depicted in Figure 4-1.

Table 4-1: Amounts of different materials used for different parts of gelatine phantom

	Water(cc)	Gelatine(gr)	Agar(gr)	Glycerol(ml)	Sigmacel(gr)
Normal	500	10	10	40	7.5
Tumour	500	10	15	40	6

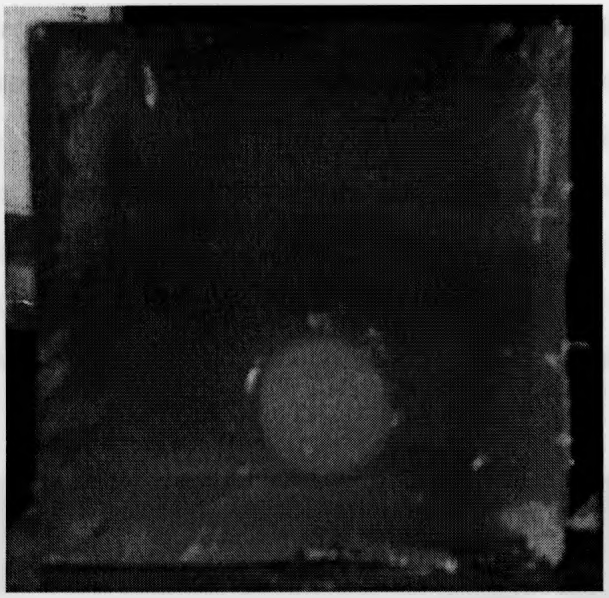

Figure 4-1: Tissue mimicking phantom with different stiff inclusion

Young's Moduli of the background and inclusion corresponding to normal and tumour areas were measured independently. This was done by using indentation tests performed on cylindrical samples obtained from the same gelatine and agar patches. The indentation system used for this purpose is an electromechanical system developed by Samani *et al*[28]. Figure 4-2 shows cylindrical samples of each region made for the indentation tests.

Figure 4-2: Gelatin and agar samples constructed for indentation process

4.2. Force Data Acquisition System and Experimental Setup

In section 3.4, various methods used in this project for stress distribution calculation were described. In each method it was assumed that force distribution on the tissue surface is available. Once measured, these force values can be substituted in Eq. 3-33 or fed into a

NN to compute the stress field. In section 3.4.3, it was stated that if the specimen's size is significantly larger than the US probe, which serves as tissue actuator in this project or if the boundary of the tissue is planar, linear force distribution of contact force is a reasonable assumption. This distribution can be characterized by two forces near the end of the US probe as shown in Figure 7-3. To measure these forces, a force data acquisition system was designed, which comprises two load cells attached to each side of the US probe. Figure 4-3 depicts the design of a mechanical attachment of the force data acquisition system.

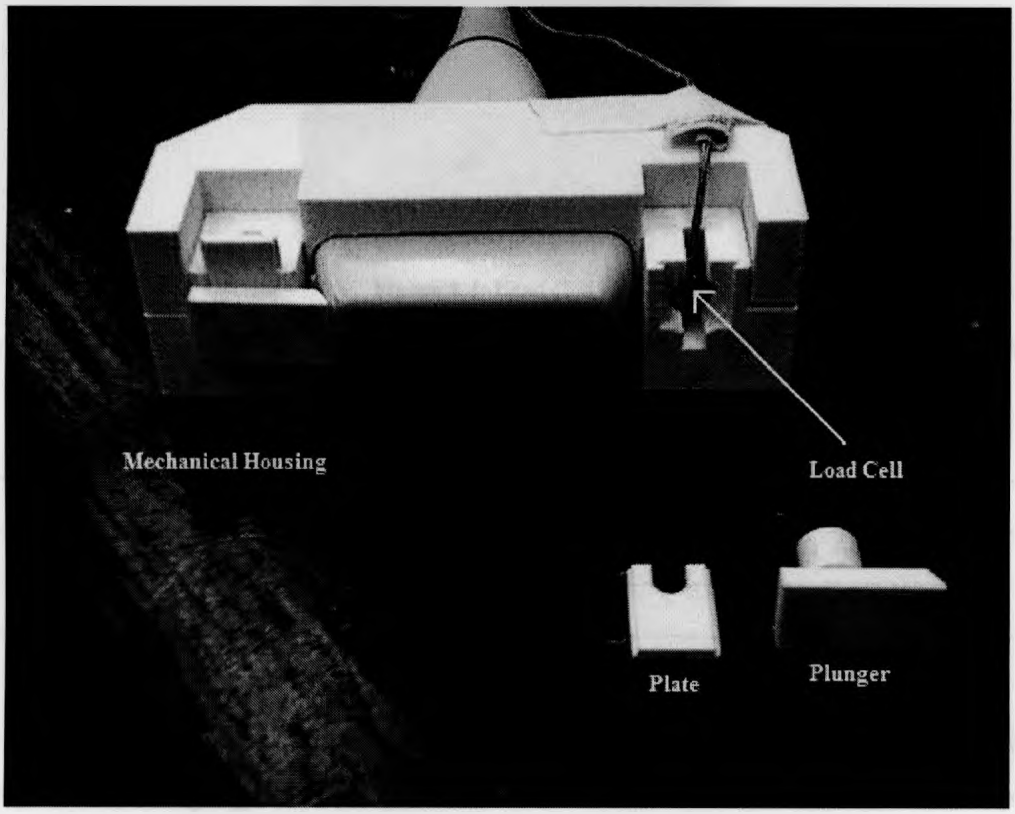

Figure 4-3: Mechanical part of the data acquisition system

The mechanical attachment of the system comprises a housing attached to US probe, which holds the load cells to the sides of the probe tightly. The plungers shown in the figure transmit the applied forces from via contact to the load cells. The plungers' asymmetric shape seen in the figure was designed to fit them into the housing and to

prevent rotation. A plate was used to prevent the plungers from falling off when the probe is in an upside down position.

The load cells used in the force data acquisition system are model LCKD-1Kg (Omega Engineering, Inc). Figure 4-4 shows one of the load cells used in the system.

Figure 4-4: Load Cell LCKD-1Kg

Table 4-2 describes the characterization of each load cell when excited with 5.000 Vdc.

Table 4-2: Load cell characterizations

Sensitivity	5.6156 mVdc
Input Resistance	379.70 Ohms
Output Resistance	355.70 Ohms

Once force is applied to a load cell, it generates an output voltage proportional to the tension of its strain gauges resulting from the force. This voltage has to be measured and converted to its corresponding force value. For data sampling, a half/full bridge analog input device, NI 9237 (National Instruments Corporation) was used to sample the generated voltage over time. The NI 9237 device is capable of measuring up to four bridge-based sensors simultaneously and provides high-speed and broad-bandwidth sampling rate. RJ50 adaptor (National Instruments Corporation) was used to connect each load cell to one channel of the NI 9237 device. Figure 4-5 shows the force data acquisition system of the experimental setups.

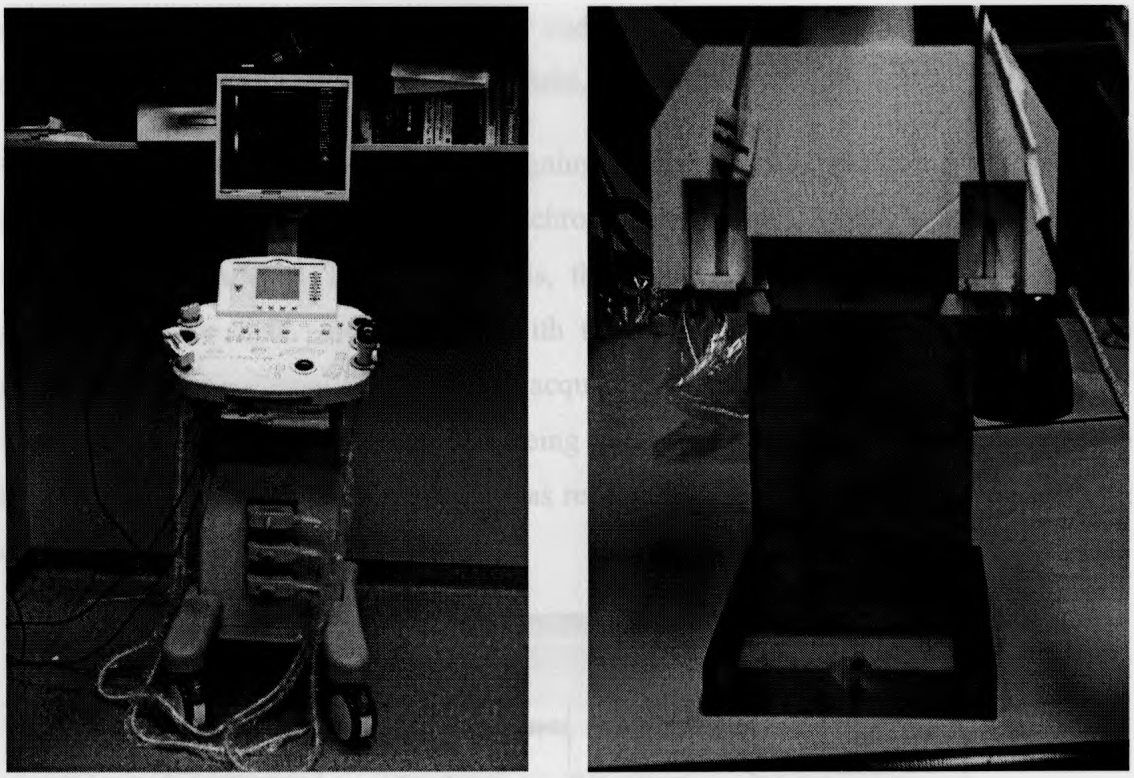

(a) (b)

(c)

Figure 4-5: (a) Sonix RP ultrasound machine (b) US probe with load cells attached to it with a tissue mimicking phantom ready for testing (c)NI9237: each load cell is connected to one channel of this device

LabVIEW (National Instruments Corporation), a commercial software package was used to facilitate communication with the NI 9237 device. When the force was applied on each load cell, generated voltage was measured by the NI 9237 device. This measured data

was stored in a text file using a LabVIEW code. This voltage data was later converted to force data using a MATLAB (The Mathworks, Inc.) code.

One of the challenges encountered in designing the force data acquisition system was that the load cell measurements had to be synchronized with the US images acquired by the Sonix RP US machine. To facilitate this, the load cells were excited using a pulse generated by the BNC port included with the Sonix RP machine. The pulses were generated at the beginning of each frame acquisition. Therefore, the load cells registered values only when an image frame was being generated while they registered no values during the time where the US machine was reconstructing images. Figure 4-6 shows the synchronization process.

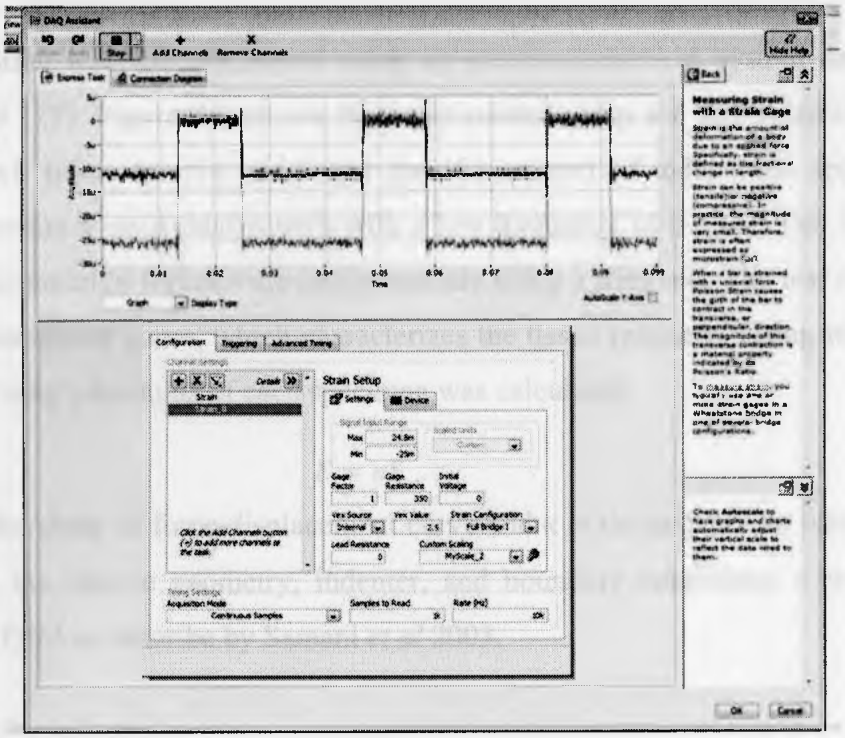

Figure 4-6: Process used for image and force data acquisition synchronization

The rate of image acquisition of the US machine depends upon various parameters such as the frequency, sector of FOV, depth, etc. With the setting pre-defined for breast ultrasound imaging in the US machine, the frame rate was 30 Frame/sec. The sampling rate of NI 9237 was set to 1 kHz. Therefore the number of force measurement data points

measured by each load cell was around 333 samples per second. The average value of these sampled data points was computed to obtain forces F_1 and F_2 applied on the tissue surface. These values characterize the contact force linear distribution, which were fed to the stress distribution calculation method described earlier.

4.3. Indentation Experiment

As described earlier, a phantom was constructed to validate the proposed elastography system. This phantom comprised two different types of material: gelatine and agar. To measure Young's Modulus of each type, small cylindrical samples were constructed to undergo indentation test.

The indentation test was performed using an electromechanical system developed by Samani *et al* [28]. Figure 4-7 shows the experimental setup for this indentation test. In this test, each tissue sample underwent specific amount of indentation applied to the sample following a sinusoidal pattern with a low frequency of 0.5 Hz. This loading was applied while reaction forces were being measure using a load cell. The test's output was a force-displacement curve, which characterizes the tissue response. Using following the equation, Young's modulus of each specimen was calculated:

$$E = \kappa S \qquad \text{Eq. 3-45}$$

where S is the slope of force-displacement curve and κ is the conversion factor that only depends on the sample geometry, indenter, and boundary conditions. κ can be found using using FEM as describe by Samani *et al* 2003.

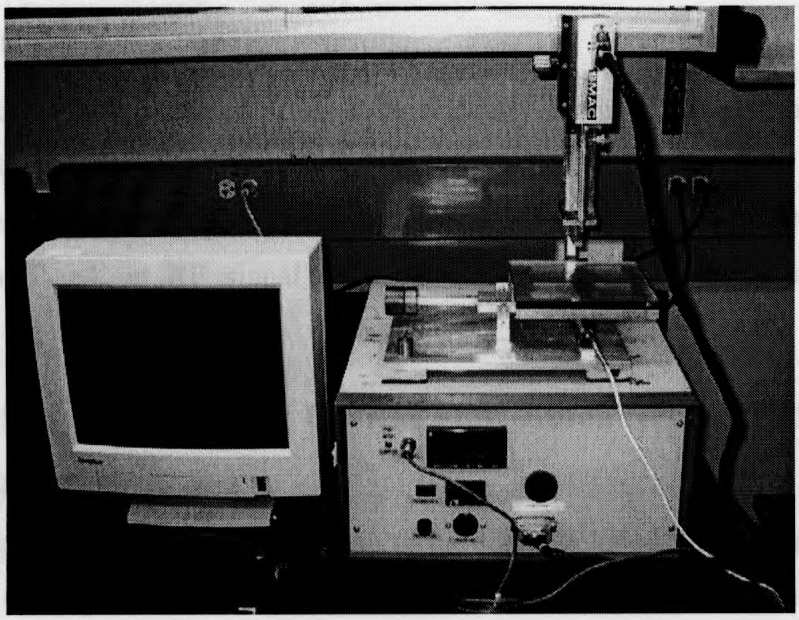

Figure 4-7: Indentation apparatus used to measure Young's modulus of tissue cylindrical samples

5. Results

In this chapter results obtained from each elasticity reconstruction technique in this project will be presented. This chapter includes numerical validation for elasticity reconstruction technique based on Optical Flow, Experimental validation elasticity reconstruction based on RF signal cross-correlation technique and indentation tests results.

5.1. Numerical Validation for Optical Flow Based Reconstruction Technique

For validating the elasticity reconstruction technique developed in conjunction with the Optical Flow displacement data acquisition method, first a breast FE model was created. This model undergoes a specific of deformation consistent with a typical US probe pressure. This FE model represents a numerical breast phantom, which was created using ABAQUS (Dassault Systèmes Simulia Corp.) as shown in Figure 5-1. The FE mesh of this phantom was constructed using a modified transfinite interpolation technique described by O'Hagan and Samani[43].

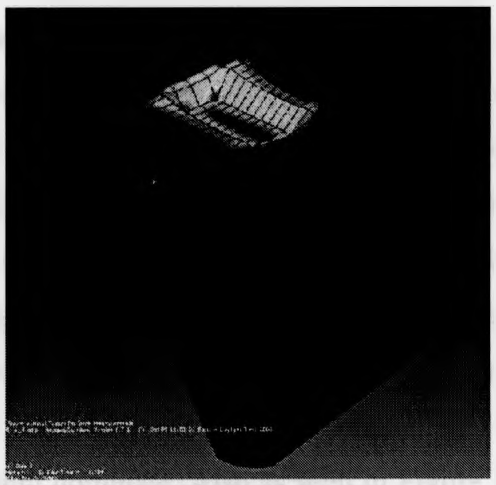

Figure 5-1: FEM of the breast

The displacements field resulting from the probe compression was computed by ABAQUS and used to generate synthetic pre- and post- compression images. Pre- and post-compression images were generated by salt and pepper noise in a way that they

resemble ultrasound images. Once these two images were constructed, they were fed to the optical flow algorithm developed in this research to compute displacement values for each pixel in the pre-compression image. Nodal displacements were then computed using interpolation functions and transferred to the FE space. Since the loading values on the surface are known, they were fed to the Boussinesq analytical model, described in Section 3.4.1, to calculate the stresses in the centre of each element in the FE model. The reconstructed values of the Young's modulus of the normal tissue and the suspicious area are given in Table 5-1.

Table 5-1: Reconstructed values for different type of the tissues

	Real Values(kPa)	Reconstructed Values(kPa)
Normal Tissue	3.25	3.25±0.45
Suspicious Area	16.25	10.35±2.00

This indicates an average error of 36% in the tumour's reconstructed Young's modulus value. This error is attributed to the limited accuracy that the Boussinesq analytical model can provide in addition to displacements errors due to the optical flow algorithm. Note that these results still indicate very significant improvement over the strain imaging technique as it shows an error of 43.2%. In the second reconstruction technique developed to improve the reconstructed tumour to normal tissue Young's modulus ratio, the procedure based on Eshelby equations described in Section 3.4.1 was used. In the optimization procedure, an interval of 0.1 to 10 was considered for the the Golden Section Search (GSS) algorithm to calculate K. This procedure led to a value of $K = 3.57$. Compared to the true K value of 5, this result shows an error of 28.6%. This shows that despite using a more accurate stress calculation model, the displacements errors due to the optical flow algorithm dominate. Also as seen in Figure 5-2(a), the tumour area is successfully detected by this method. Compared to an Elastogram (strain image) shown in Figure 5-2(b) obtained from conventional US elastography, the quality of Young's modulus image constructed by the proposed method is significantly better.

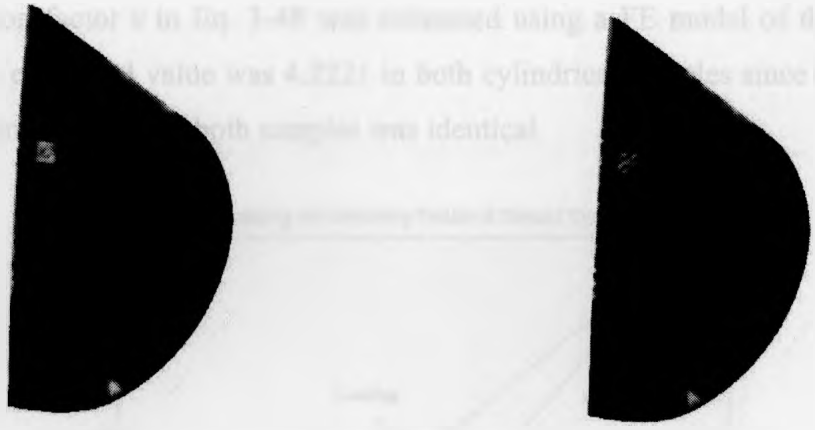

(a) (b)

Figure 5-2: (a) Elastogram using the micromechanics based method (b) Elastogram using conventional strain imaging method

This numerical study indicates the potential of proposed method in developing a real-time US elastography system to detect suspicious areas and reconstruct its Young's Modulus for diagnostic purposes.

5.2. Indentation Test Results for Gelatin Phantom Samples

As mentioned earlier, gelatin and agar samples of each tissue type in the tissue mimicking phantom was constructed. Each was a cylindrical shape specimen that underwent a sinusoidal indentation with 1mm amplitude and 0.5 Hz frequency. Resulting reaction forces were measured by the load cell of the indentation apparatus. Figure 5-3 and Figure 5-4 illustrate the force-displacement curves obtained from testing the gelatin and agar samples, respectively. Table 5-2 shows the slope values of the force-displacement curve and the corresponding Young's modulus values of each tissue type.

Table 5-2: Indentation results for each type of tissues

	Slope (N/mm)	Young's Modulus(kPa)
Normal Tissue	5.2	22.1
Suspicious area	7.5	31.5

The conversion factor κ in Eq. 3-48 was estimated using a FE model of the cylindrical samples. The estimated value was 4.2221 in both cylindrical samples since the geometry of cylinders and indenter in both samples was identical.

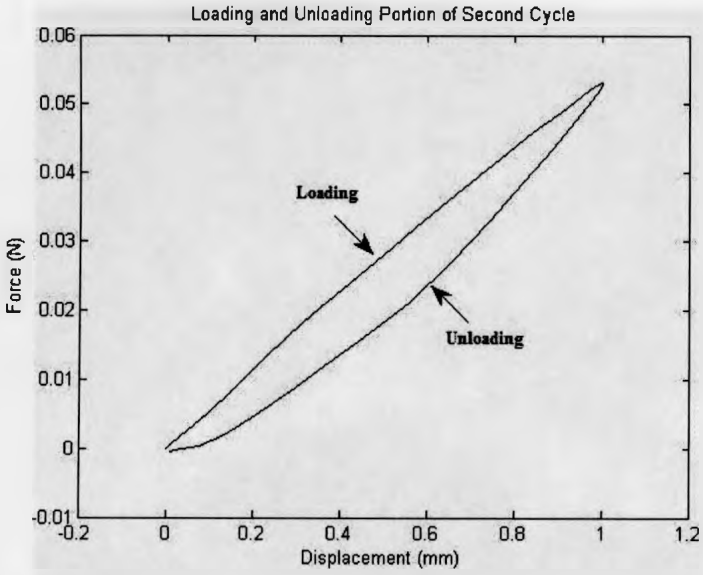

Figure 5-3: Force-Displacement curve for the gelatinous tissue

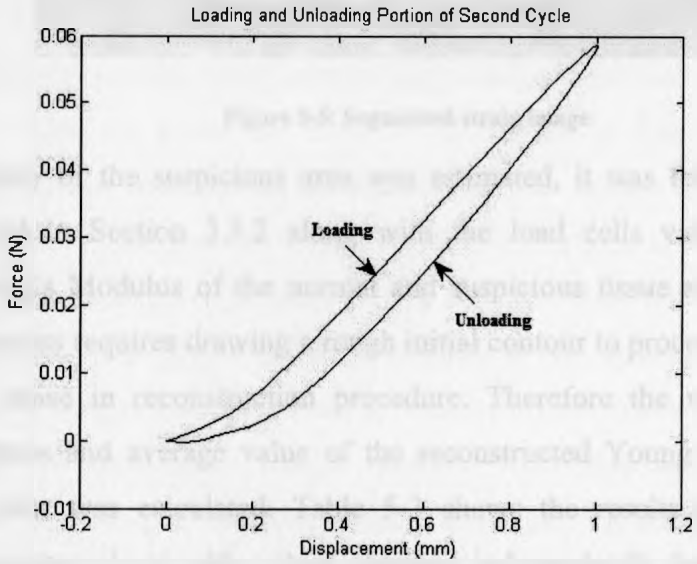

Figure 5-4: Force-Displacement curve for the agar tissue sample

5.3. Experimental Results of the RF signal Cross-correlation Based Technique

Figure 5-5 shows segmented strain image of the phantom obtained by DDC.

Figure 5-5: Segmented strain image

Once the boundary of the suspicious area was estimated, it was fed into the iterative process described in Section 3.5.2 along with the load cells values F_1 and F_2 to reconstruct Young's Modulus of the normal and suspicious tissue areas. Note that the segmentation process requires drawing a rough initial contour to proceed. This introduces undeterministic noise in reconstruction procedure. Therefore the whole process was performed 20 times and average value of the reconstructed Young's moduli with the corresponding error was calculated. Table 5-3 shows the results obtained from the reconstruction process along with values obtained independently from the indentation tests.

Table 5-3: Reconstruction results for each type of the tissue

	Real Value(kPa)	Reconstructed Value(kPa)	Error (%)
Normal Tissue	22.1	22.7	2.4
Suspicious area	31.5	33.3	5.7

The value of the load cell forces, which were measured using the force data acquisition system were $F1 = 25.5gr$ and $F2 = 23.5gr$. These forces were applied on the boundary of the tissue mimicking phantom.

5.4. Sensitivity Analysis for Tumour Location

In section 3.5.2, a method to estimate Young's modulus of the normal tissue was proposed. This method involves measuring the strain values from the strain image and computing the stress components of upper elements in the FE model of a homogeneous material with arbitrary Young's Modulus but same geometry and loading distribution on the surface. This method provides accurate results when the tumours are not excessively stiff and are located deeper within the tissue. Since in real cases, suspicious areas tend to be stiffer than the surrounding tissue, accuracy of stresses calculated using the proposed technique may suffer. To assess the accuracy in relation to this issue, a sensitivity analysis was performed by varying the stiffness of the tumour area relative to the background. It was assumed that the tumour location is confined in the one bottom third of the phantom. The location of tumour, its size and its Young's modulus were varied systematically. Figure 5-6 shows different location of the tumour as well as upper elements in the FE model that were used to reconstruct background tissue's Young's modulus. Table 5.4 summarizes results obtained from this analysis. It is worth mentioning that this analysis confirmed that the deeper the tumour, the better the background tissue's Young's Modulus estimation.

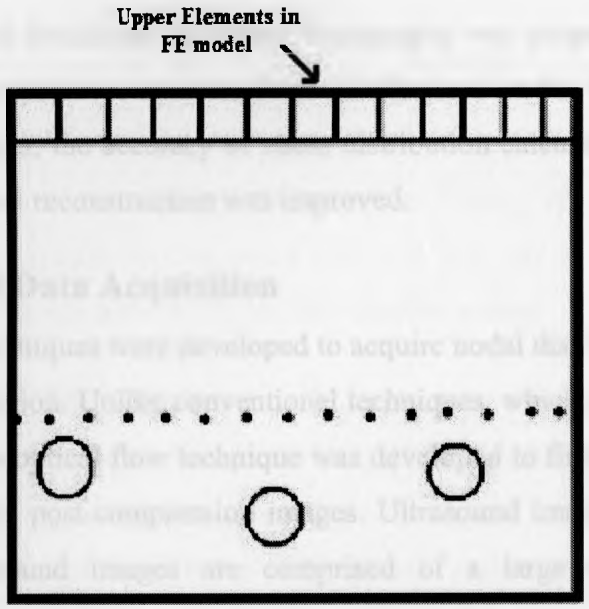

Figure 5-6: Different locations of the tumour

Table 5-4 shows the maximum and average error in the reconstructed normal tissue's Young's modulus values. It shows a maximum error of 5.12%, which indicates that the proposed method is highly accurate for challenging elastography applications where the tumour located deep inside the organ such as breast elastography.

Table 5-4: Sensitivity Analysis for Young' Modulus value due to Homogeneity assumption

	Maximum Error (%)	Average Error (%)
Young's Modulus of normal tissue	5.12	2.37

6. Summary and Conclusion

In this project, a novel technique for breast elastography was proposed, which utilizes a force data acquisition system to measure force distributions on the breast's surface. With incorporating force data, the accuracy of stress distribution calculation using SFEM and therefore elastic moduli reconstruction was improved.

6.1. Displacement Data Acquisition

In this project two techniques were developed to acquire nodal displacement data induced by mechanical stimulation. Unlike conventional techniques, which provide only the axial displacement field, an optical flow technique was developed to find the 2D displacement field between pre- and post-compression images. Ultrasound imaging can provide such images. Since ultrasound images are comprised of a large number of speckles, conceptually one can use them as landmarks to track the displacement. Optical flow technique is capable of tracking such speckles provided that the brightness associated to speckles remains the same from pre-compression image to post-compression image.

Another approach that was taken in this project to acquire displacement data was strain imaging using cross-correlation based method. This method was readily implemented in the Sonix RP US machine available in our laboratory. Although strain images obtained from the 2D probe RF signal cross-correlation provides axial strains only, they are known to be the most accurate compared to other techniques. Research is still ongoing to develop RF signal cross-correlation techniques capable of providing accurate 2D displacements.

6.2. Force Data Acquisition

A force data acquisition system to measure the force applied on the breast surface was designed and implemented. This system contains two load cells attached tightly to the sides of US probe. The system is capable of measuring the applied forces with high accuracy. The load cells were connected to a half/full bridge device, NI 9237, to measure the induced voltage as a result of tension or compression of strain gauges in each of the load cells. Once the generated voltages by each load cell were measured, a proper

conversion factor was used to convert the induced voltages to their corresponding force values. The system is capable of measuring the value of load cells in high sampling frequency, thus allowing reduction of the noise measurement level by averaging the sampled forces.

The forces values were then used to estimate contact loading distribution on the breast surface. A linear distribution was assumed provided that the surface of the breast is relatively larger than the US probe or the surface itself is planar.

6.3. Reconstruction Techniques

Two techniques were proposed to reconstruct Young's modulus of normal and suspicious tissues. The output of both techniques is the absolute value of Young's Muduls and their ratio. Each technique comprises different displacement data acquisition system but both require the loading data applied on the surface.

In the first proposed technique, the optical flow method was applied to acquire displacement field between pre- and post-compression images. Strain tensors were then computed by differentiation of the estimated displacement field. The loading distribution was estimated using the data acquisition system developed in this research, and was fed into two different analytical models to compute stresses at the centre of each element in the breast model. The first method of computing stress distribution involved computing stress components using the analytical solution proposed by Boussinesq. The second method involved updating the ratio of Young's modulus of the tumour to the normal tissue using strain tensors in homogeneous specimen using an analytical micromechanics based method proposed by Lui *et al* [13]. Once stress distribution was calculated using either method, simple Hook's law equation was used to reconstruct Young's modulus of each element in the model.

In the second proposed reconstruction technique, axial strain images acquired by the Ultrasonix RP machine using cross-correlation techniques were used. Loading distribution was estimated using measured contact forces on the surface. To calculate stresses in this technique, a SFEM technique involving two different NNs to construct

two main models was used. The first NN was trained with uniform constant loading on the surface where the tumour location, Young's Modulus of each type of tissue and tumour geometry was randomly altered to take into account these parameters variation. The second NN was trained with ramp loading applied on the surface while varying the same parameters as in the previous NN. The inputs of each NN comprise the tumour geometry and Young's Modulus of each tissue. Once the reaction forces were measured, linear combination of these two main modes computed the stress distribution. In this technique, Eq. 2-11 was used iteratively to reconstruct the ratio of the Young's Moduli. Once the ratio was reconstructed, the stress field corresponding to a homogeneous medium was used in conjunction with the actual strain tensors for upper elements in the FE model to find Young's modulus of normal tissue. This was used along with the previously calculated ratio to determine the tumour's Young's modulus.

6.4. Numerical Simulations and Tissue Mimicking Phantom Study

To validate the proposed methods, simulations were first performed on the numerical breast phantom shown in Figure 32-5. The phantom was numerically deformed using a FE model. Pre- and post-compression images were then constructed using nodal positions and speckle noise. To obtain displacement data, a hierarchical framework of optical flow acting on pre- and post-compression was used to estimate the displacement field, thus the strain tensors. Stress distribution was, then, calculated using analytical models. The results showed the feasibility of using optical flow in tissue deformation acquisition application. The reconstruction error was 36% when the stress distribution was calculated using Boussinesq theorem while it was reduced to 28.6% when a more accurate micromechanics based was used to calculate the stress field. The errors can be attributed to two major sources: displacements errors obtained from the flow algorithms and stress field errors. It may be speculated that the former is dominant. At any rate, the obtained elasticity image depicted in Figure 5-2 shows promising results. The tumour tissue was effectively detected and the accuracy of the reconstructed Young's modulus may be acceptable for diagnostic purposes.

For tissue mimicking phantom study, a gelatine/agar phantom shown in Figure 4-1 was constructed to validate the proposed technique. The second reconstruct approach that involved using the US acquired axial displacements in conjunction with SFEM. As reported in Section 5.3, the reconstruction results were very promising while the methods retain the real-time aspect of image reconstruction. Also, sensitivity analysis was performed, which showed that the deeper the tumour within the tissue, the better the estimation of the normal tissue's Young's Modulus leading to more accurate reconstruction.

6.5. Pros and Cons of the Proposed Methods

This section is dedicated to discuss the pros and cons of the proposed methods. While the proposed methods are real-time, there are issues associated with each approach.

6.5.1. Pros of the Methods

In this project, two real-time techniques were proposed to reconstruct Young's modulus of soft tissue and potential suspicious areas. In the first approach, analytical models were utilized to compute the stress field. In fact this method can be considered as a real-time unconstrained elastography method. Unlike other elastography techniques that incorporate only the axial displacement field, optical flow was used, which is capable of estimating 2D displacement field. Exploiting the 2D displacement field in principle should increase the accuracy of the reconstruction and reduce errors provided that the motion tracking technique is sufficiently accurate. In the second technique, SFEM was applied to calculate the stress field for real-time and accurate Young's modulus reconstruction. Unlike the first technique, the second technique can be categorized as constrained elastography techniques in which that the elastic modulus within each tissue volume was assumed to be uniformly distributed.

6.5.2. Cons of the Methods

One of the difficulties encountered in the first proposed technique was that when compression was applied on the phantom's surface, the speckle patterns changed. These changes introduced errors in the optical flow tracking technique. The reason is that as

mentioned in Section 3.1.1, the main equation governing the optical flow techniques was Motion Constraint Equation, which assumes that the brightness associated with each speckle remains constant from pre-compression image to post-compression image. Unfortunately, this was not the case, and as a result the accuracy of the calculated displacement field suffered. Furthermore, optical flow techniques have intrinsic issues associated with approximating derivatives of the image intensity leading to extra reconstruction errors. Another drawback that pertains to the second elastography technique was lateral displacements were not available as the current cross correlation techniques are not well developed to estimate them in real-time.

6.6. Future Directions

In this work, novel imaging systems were developed for breast cancer assessment. At this point, a proof of concept was provided as the methods were tested and their feasibility and accuracy were demonstrated based on numerical and tissue mimicking phantom experiments. Future research work may involve the following:

- Developing fully online reconstruction system: parts of the system involve offline processing such as system calibration, retrieving force data, etc. The system can be further developed to coordinate all of steps from data acquisition and elastic modulus reconstruction using a more sophisticated LabVIEW program.
- Improving optical flow: for this purpose work is under way in our group to incorporate Navier equations as an additional constraint.
- Incorporating incompressibility of soft tissues to compute lateral displacements: to this end, Lubinski *et al* [15] proposed a technique to compute displacement field in lateral direction by having axial displacement field and incorporating the incompressibility constrains. This technique may be implemented and used in the first proposed system.
- Assuming multiple lesions in the phantom studies: in the present work, a simple case of having one lesion was used to validate the proposed methods. To assess the effectiveness of these techniques with multi-focal cancer types,

future developments may consider multiple lesions with random dimensions and locations.

- Real patient study: one of the future developments may involve real breast cancer patient's study where clinicians and patients can provide feedback on the system's performance and utility.
- Improving the force distribution estimation: In order to improve stress field calculation more accurate contact force distribution may be considered instead of the linear load distribution used in the present work.

Appendix A: Transfinite Interpolation

The TFI approach to grid generation is based on the concept of mapping a computational domain C (logical space) into a closed and bounded region defined in the physical domain P. TFI is simple to implement and only requires a unique mapping between the boundaries of the two domains $\vec{F}: \partial C \rightarrow \partial P$ be defined.

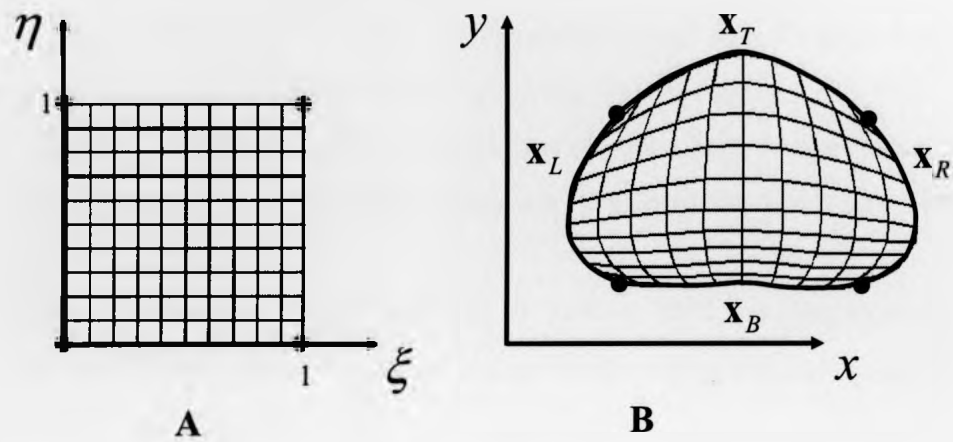

Figure 1-i : A unit square (logical space) (A). A prostate shaped physical space (B)

In 2D C is in the form of the unit square, i.e. $C(\xi,\eta) \in [0,1]$. The mapping function $\vec{F}$ is built by partitioning ∂P into four curves parameterized using the coordinates of ∂C as shown in Figure 1-i:

$$\begin{aligned} \boldsymbol{X}_L &= (x_L, y_L) = \vec{F}(0,\eta) \quad & \boldsymbol{X}_R &= (x_R, y_R) = \vec{F}(1,\eta) \\ \boldsymbol{X}_B &= (x_B, y_B) = \vec{F}(\xi,0) \quad & \boldsymbol{X}_T &= (x_T, y_T) = \vec{F}(\xi,1) \end{aligned} \qquad \text{Eq. A-1}$$

that are joined at four corners denoted by:

$$\begin{aligned} \boldsymbol{X}_{TR} &= (x_{TR}, y_{TR}) = \vec{F}(1,1) \quad & \boldsymbol{X}_{BR} &= (x_{BR}, y_{BR}) = \vec{F}(1,0) \\ \boldsymbol{X}_{TL} &= (x_{TL}, y_{TL}) = \vec{F}(0,1) \quad & \boldsymbol{X}_{BL} &= (x_{BL}, y_{BL}) = \vec{F}(0,0) \end{aligned} \qquad \text{Eq. A-2}$$

Using $\vec{F}$ in Eq. A-1, we can now construct a TFI mapping function from C to P using the vector-valued bilinear blended map:

$$\boldsymbol{X} = (\xi,\eta) = \begin{bmatrix} x(\xi,\eta) \\ y(\xi,\eta) \end{bmatrix} = \begin{matrix} (1-\eta)\boldsymbol{X}_B + \eta\boldsymbol{X}_R + (1-\xi)\boldsymbol{X}_T \\ +\xi\boldsymbol{X}_R - \xi\eta\boldsymbol{X}_{TR} - \xi(1-\eta)\boldsymbol{X}_{BR} \\ -\eta(1-\xi)\boldsymbol{X}_{TL} - (1-\xi)(1-\eta)\boldsymbol{X}_{BL} \end{matrix} \qquad \text{Eq. A-3}$$

In order to generate the vertices of a grid over the closed shape in Cartesian domain P (Figure A-1 B) and $N * N$ computational grid $\boldsymbol{X}_c = \left(i.\frac{1}{N-1}, j.\frac{1}{N-1}\right)$, $i, j = 0,1, \ldots, N-1$ is defined and then mapped into P using Eq. A-3. It is important to note that when $\boldsymbol{X}_c$ a rectilinear grid is. This technique only requires that $\vec{F}$ be defined for the vertices on the outer surface of $\boldsymbol{X}_c$.

References

[1] S. Baker and I. Matthews. 2004, Lucas-kanade 20 years on: A unifying framework. *International Journal of Computer Vision 56(3),* pp. 221-255.

[2] J. L. Barron, D. J. Fleet and S. S. Beauchemin. 1994, Performance of optical flow techniques. *International Journal of Computer Vision 12(1),* pp. 43-77.

[3] J. L. Barron and M. Khurana. 1997, Determining optical flow for large motions using parametric models in a hierarchical framework. *Vision Interface (VI1997)*

[4] J. L. Barron. Experience with 3D optical flow on gated MRI cardiac datasets. Presented at Proceedings - 1st Canadian Conference on Computer and Robot Vision, may 17, 2004 - may 19.

[5] J. Bishop, A. Samani, J. Sciarretta and D. B. Plewes. 2000, Two-dimensional MR elastography with linear inversion reconstruction: Methodology and noise analysis. *Phys. Med. Biol. 45(8),* pp. 2081-2091.

[6] I. Cespedes, J. Ophir, H. Ponnekanti and N. Maklad. 1993, Elastography: Elasticity imaging using ultrasound with application to muscle and breast in vivo. *Ultrason. Imaging 15(2),* pp. 73-88.

[7] M. M. Doyley, Q. Feng, J. B. Weaver and K. D. Paulsen. 2007, Performance analysis of steady-state harmonic elastography. *Phys. Med. Biol. 52(10),*

[8] B. K. P. Horn and B. G. Schunck. Determining Optical Flow. Artificial Intelligence Journal, 1981, 185-203

[9] F. Kallel and M. Bertrand. Quantitative strain imaging and elasticity reconstruction. Presented at Part 2 (of 2), September 20, 1995 - September 23.

[10] H. Karimi, A. Fenster and A. Samani. A real-time method for breast cancer diagnosis using optical flow. Presented at Medical Imaging 2009: Biomedical Applications in Molecular, Structural, and Functional Imaging, February 8, 2009 - February 10.

[11] I. Khalaji, K. Rahemifar and A. Samani. Statistical finite element analysis. Engineering in Medicine and Biology Society, 2008. EMBS 2008. 30th Annual International Conference of the IEEE

[12] I. Khalaji, K. Rahemifar and A. Samani. Accelerated statistical shape model-based technique for tissue deformation estimation. Presented at SPIE Medical Imaging 2009: Biomedical Applications in Molecular, Structural, and Functional Imaging, February 8, 2009 - February 10.

[13] H. T. Liu, L. Z. Sun, G. Wang and M. W. Vannier. 2003, Analytic modeling of breast elastography. *Med. Phys. 30(9),* pp. 2340-2349.

[14] Y. Liu, S. Chen, C. Lin, C. Huang and Y. Sun. Motion tracking on elbow tissue from ultrasonic image sequence for patients with lateral epicondylitis. Presented at 29th Annual International Conference of IEEE-EMBS, Engineering in Medicine and Biology Society, EMBC'07, August 23, 2007 - August 26.

[15] M. A. Lubinski, S. Y. Emelianov, K. R. Raghavan, A. E. Yagle, A. R. Skovoroda and M. O'Donnell. 1996, Lateral displacement estimation using tissue incompressibility. *IEEE Trans. Ultrason. Ferroelectr. Freq. Control 43(2),* pp. 247-256.

[16] B. D. Lucas and T. Kanade. Iterative Image Registration Technique with an application to stereo vision, Proceeding of Imaging Understanding Workshop, pp. 121-130 (1981)

[17] E. L. Madsen, M. A. Hobson, H. Shi, T. Varghese and G. R. Frank. 2005, Tissue-mimicking agar/gelatin materials for use in heterogeneous elastography phantoms. *Phys. Med. Biol. 50(23),* pp. 5597-5618.

[18] G. E. Mailloux, A. Bleau, M. Bertrand and R. Petitclerc. 1987, Computer analysis of heart motion from two-dimensional Echocardiograms *IEEE Transactions on Biomedical Engineering BME-34(5),* pp. 356-364.

[19] H. Mehrabian, H. Karimi and A. Samani. Accurate optical flow field estimation using mechanical properties of soft tissues. Presented at SPIE Medical Imaging 2009: Biomedical Applications in Molecular, Structural, and Functional Imaging, February 8, 2009 - February 10.

[20] M. I. Miga. 2003, A new approach to elastography using mutual information and finite elements. *Phys. Med. Biol. 48(4),* pp. 467-480.

[21] H. Nagel. 1983, Displacement vectors derived from second-order intensity varation in imaging sequences. *Computer Vision, Graphics, and Image Processing 21(1),* pp. 85-117.

[22] M. O'Donnell, S. Y. Emelianov, A. R. Skovoroda, M. A. Lubinski, W. F. Weitzel and R. C. Wiggins. Quantitative elasticity imaging. Presented at Proceedings of the IEEE 1993 Ultrasonics Symposium, October 31, 1993 - November 3.

[23] J. Ophir, I. Cespedes, B. Garra, H. Ponnekanti, Y. Huang and N. Maklad. 1996, Elastography: Ultrasonic imaging of tissue strain and elastic modulus in vivo. *European Journal of Ultrasound 3(1),* pp. 49-49.

[24] D. B. Plewes, J. Bishop, A. Samani and J. Sciarretta. 2000, Visualization and quantification of breast cancer biomechanical properties with magnetic resonance elastography. *Phys. Med. Biol. 45(6),* pp. 1591-1610.

[25] H. Ponnekanti, J. Ophir and I. Cespedes. 1994, Ultrasonic imaging of the stress distribution in elastic media due to an external compressor. *Ultrasound in Medicine and Biology 20(1),* pp. 27-33.

[26] A. Samani, J. Bishop and D. B. Plewes. 2001, A constrained modulus reconstruction technique for breast cancer assessment. *IEEE Trans. Med. Imaging 20(9),* pp. 877-885.

[27] A. Samani, J. Bishop, M. J. Yaffe and D. B. Plewes. 2001, Biomechanical 3-D finite element modeling of the human breast using MRI data. *IEEE Trans. Med. Imaging 20(4),* pp. 271-279.

[28] A. Samani, J. Bishop, C. Luginbuhl and D. B. Plewes. 2003, Measuring the elastic modulus of ex vivo small tissue samples. *Phys. Med. Biol. 48(14),* pp. 2183-2198.

[29] A. Samani, J. Zubovits and D. Plewes. 2007, Elastic moduli of normal and pathological human breast tissues: An inversion-technique-based investigation of 169 samples. *Phys. Med. Biol. 52(6),* pp. 1565-1576.

[30] A. R. Skovoroda, S. Y. Emelianov and M. O'Donnell. 1995, Tissue elasticity reconstruction based on ultrasonic displacement and strain images. *IEEE Trans. Ultrason. Ferroelectr. Freq. Control 42(4),* pp. 747-765.

[31] A. R. Skovoroda, S. Y. Emelianov, M. A. Lubinski, A. P. Sarvazyan and M. O'Donnell. 1994, Theoretical analysis and verification of ultrasound displacement and strain imaging. *IEEE Trans. Ultrason. Ferroelectr. Freq. Control 41(3),* pp. 302-313.

[32] A. R. Skovoroda, M. A. Lubinski, S. Y. Emelianov and M. O'Donnell. 1998, Nonlinear estimation of the lateral displacement using tissue incompressibility. *IEEE Trans. Ultrason. Ferroelectr. Freq. Control 45(2),* pp. 491-503.

[33] R. Souchon, L. Soualmi, M. Bertrand, J. Chapelon, F. Kallel and J. Ophir. 2002, Ultrasonic elastography using sector scan imaging and a radial compression. *Ultrasonics 40(1-8),* pp. 867-871.

[34] S. Sun, D. Haynor and Y. Kim. Motion estimation based on optical flow with adaptive gradients. Presented at International Conference on Image Processing (ICIP 2000), September 10, 2000 - September 13.

[35] E. Turgay, S. Salcudean and R. Rohling. 2006, Identifying the mechanical properties of tissue by ultrasound strain imaging. *Ultrasound in Medicine and Biology 32(2),* pp. 221-235.

[36] T. Varghese, J. Ophir and F. Kallel. 1997, Theoretical framework for elastographic imaging: The strain filter. *Ultrasound in Medicine and Biology 23*pp. PIO 7412-PIO 7412.

[37] R. Zahiri-Azar and S. E. Salcudean. 2006, Motion estimation in ultrasound images using time domain cross correlation with prior estimates. *IEEE Transactions on Biomedical Engineering 53(10),* pp. 1990-2000.

[38] R. Zahiri-Azar and S. E. Salcudean. 2006, P1A-3 real-time estimation of lateral displacement using time domain cross correlation with prior estimates. *Ultrasonics Symposium, 2006. IEEE* pp. 1209-1212.

[39] A. Zaim. Automatic segmentation of the prostate from ultrasound data using feature-based self organizing map. Presented at 14th Scandinavian Conference on Image Analysis, SCIA 2005, June 19, 2005 - June 22.

[40] Q. Zhu, Y. Jiang, J. Liu, H. Liu, Q. Sun, Q. Dai and X. Chen. (2008, Real-time ultrasound elastography: Its potential role in assessment of breast lesions. *Ultrasound in Medicine and Biology 34(8),* pp. 1232-1238.

[41] S. Lobregt, M.A. Viergever, 1995, A Discrete Dynamic Contour Model, IEEE Transaction on Medical Imaging Vol.14, No.1

[42] A.C. Fischer-Cripps, Introduction to Contact Mechanics, Springer 2007, 2nd Edition

[43] J. O'Hagan, A. Samani, Measurement of the hyperelastic properties of tissue slices with tumour inclusion, *Physics in Medicine and Biology*, v 53, n 24, p 7087-7106, December 21, 2008

[44] Walker, W.F., Trahey, G.E., A fundamental limit on the performance of phase aberrationcorrection and correlation based flow estimates in medical ultrasound, Ultrasonics Symposium, 1993. Proceedings., IEEE 1993, 1149-1153 vol.2

[45] Foster, G.C., Embree, M.P. and O'Brien, W.D., 1990. Flow velocity profile via time-domain correlation: error analysis and computer simulation. *IEEE Trans Ultrasound Ferroelectric Freq Control*, pp. 164–174 UFFC-37

[46] Parris Saxon Wellman, Tactile Imaging, Harvard University, May 1999

[47] http://www.cancer.ca/